2010

Optimization of a ball-milled photocatalyst for wastewater treatment through use of an orthogonal-array experimental design

Bradley J. Ridder
University of South Florida

Optimization of a Ball-Milled Photocatalyst for Wastewater Treatment Through Use of an Orthogonal-Array Experimental Design

by

Bradley J. Ridder

A thesis submitted in partial fulfillment
of the requirements for the degree of
Master of Science in Chemical Engineering
Department of Chemical and Biomedical Engineering
College of Engineering
University of South Florida

Major Professor: John T. Wolan, Ph.D.
Vinay K. Gupta, Ph.D.
D. Yogi Goswami, Ph.D.
John N. Kuhn, Ph.D.

Date of Approval:
March 31, 2010

Keywords: indium vanadate, $InVO_4$, titania, TiO_2, amorphous precursor, methyl orange, Taguchi methods

"Knowledge brings the sting of disillusionment, but the pain teaches perspective."

-Wizards of the Coast

Acknowledgments

First and foremost, I would like to acknowledge my adviser, Dr. John T. Wolan, for his helpful ideas, guidance, and allaying my (many...!) fears that arose during the course of my graduate school experience. I would also like to thank my committee members, Dr. Vinay Gupta, Dr. John Kuhn, and Dr. Yogi Goswami. The expertise of Dr. Cecil Coutinho of the USF Interfacial Phenomena Lab and Kofi Dalyrymple of the Clean Energy Research Center was also of great help. I would also like to thank Haitao "Eddie" Li of the USF Green Energy Systems Lab for his help with the BET measurements in this work, and Bijith Mankidy and Ajay Rajgadkar for their help with procuring the SEM-EDS results. I also thank my lab partners, current and former: Ala'a Kababji, Chris Monteparo, Ali Syed Gardezi, William Bosshart, and Sandra Pettit. Their words of encouragement, intelligent conversations, and helpful advice were a memorable part of my graduate school experience. Lastly, I would like to acknowledge Mirko Hrovat, who posted his baseline-fitting routine on the MATLAB Central File Exchange, without which the UV spectra in this work would have been much more difficult to analyze. Thanks! :)

Table of Contents

List of Tables

List of Figures

Optimization of a Ball-Milled Photocatalyst for Wastewater Treatment Through Use of an Orthogonal-Array Experimental Design

Bradley James Ridder

Abstract

The effects of various catalyst synthesis parameters on the photocatalytic degradation kinetics of aqueous methyl orange dye are presented. The four factors investigated were: i) $InVO_4$ concentration, ii) nickel concentration, iii) $InVO_4$ calcination temperature, and iv) ball-milling time. Three levels were used for each factor. Due to the large number of possible experiments in a full factorial experiment, an orthogonal-array experimental design was used. UV-vis spectrophotometry was used to measure the dye concentration. The results show that nickel concentration was a significant parameter, with 90% confidence. The relative ranking of importance of the parameters was nickel concentration > $InVO_4$ concentration > $InVO_4$ calcination temperature > milling time. The results of the orthogonal array testing were used to make samples of theoretically slowest and fastest catalysts. Curiously, the predicted-slowest catalyst was the fastest overall, though both samples were faster than the previous set. The only difference between the slowest and fastest catalysts was the milling time, with the longer-milled catalyst being more reactive. From this result, we hypothesize that there is an interaction effect between nickel concentration and milling time. The slowest and fastest catalysts were characterized using energy-dispersive spectroscopy (EDS), scanning electron microscopy (SEM), x-ray powder diffractometry (XRD), BET surface area analysis, and diffuse-reflectance spectroscopy (DRS). The characterization results show that the fastest catalyst had a lower band gap than the slowest one, as well as a slightly greater pore volume and average pore diameter. The results indicate that fast kinetics are achieved with low amounts of nickel and a long ball milling time. Under the levels tested, $InVO_4$ concentration and the calcination temperature of the $InVO_4$ precursor were not significant.

Chapter 1: Design of Experiments

In this work, an orthogonal array experimental design was used to maximize the reactivity of a photocatalyst. This chapter provides the foundation for understanding design of experiments (DOE) methods and terminology. Wise use of DOE methods can drastically reduce the time and effort required to optimize processes – catalyst synthesis or otherwise. In this chapter, we discuss the general procedures for experimental design, and several common experimental designs. We then examine different data analysis techniques – the column effects method, and analysis of variance (ANOVA).

1.1 General DOE Guidelines

"Design of experiments" refers to an orderly plan, or design, that describes four key features of an experiment, as summarized by Finney [1]:

i. The factors to be tested.
ii. What test subjects will be used to investigate these factors.
iii. The rules for applying the treatments to the test subjects.
iv. What measurements will be taken during the experiment, and when they will be taken.

For each step, the experimenter should consider the impact that his or her decision(s) will have on the cost, feasibility, and precision of the experiment [1].

1.2 An Example DOE Scenario

Though good experimental design is important for producing reliable, reproducible research, many engineers are unfamiliar with DOE concepts, and the terms used in §1.1 may seem foreign. For didactic purposes, we present a simple example related to chemical engineering. Suppose a research team is investigating the reaction A → B in the bench-scale plug-flow reactor in figure 1 below:

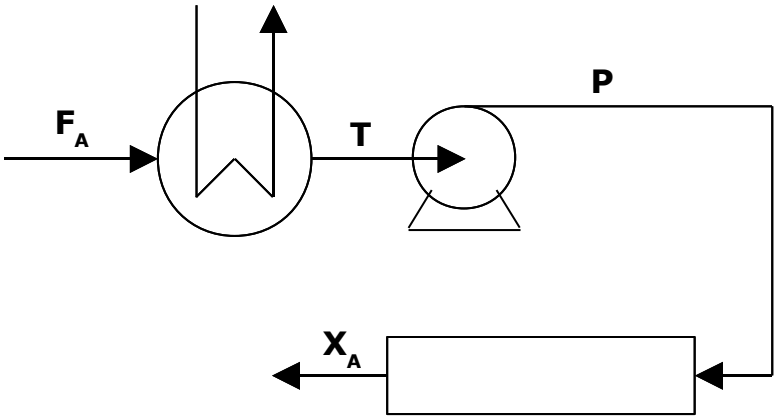

Figure 1: Reactor setup for example DOE problem.

Reactant A flows at F_A (mol/min), and is pre-heated to temperature T (K). Then it is pumped up to pressure P (bar), and reacted to form B. The conversion, X_A, is measured at the reactor's exit. The researchers want to tweak the values of T, P, and F_A to maximize X_A. The team chooses the settings of T, P, and F_A as follows, based upon their intuition and experience:

Table 1: Factors and levels for example DOE problem.

T (°C)	300	500
P (bar)	20	30
F_A (mol/min)	5	15

Using the technical vocabulary, the variables we wish to investigate, or factors, are T, P, and F_A. Our test subject, or plot, is the reactor itself. In this case we only have a single plot, but it is common to have more (e.g. testing a new fertilizer on several tobacco plants.) The different settings of the factors are called levels, and each distinct combination of levels is called a run.

To do the experiment, we measure X_A for all possible factor-level combinations. The number of required runs is the product of the number of levels for each factor; we have 3 factors, with 2 levels each: $2 \cdot 2 \cdot 2 = 2^3 = 8$. Table 2 below shows the experimental results. Though the runs here are number sequentially, it is customary to do runs in a random order as a hedge against experimenter bias [1,2].

Table 2: Experimental results for DOE example.

Run	T (K)	P (bar)	F_A (mol/min)	X_A
1	300	20	5	0.196
2	300	20	15	0.345
3	300	30	5	0.256
4	300	30	15	0.470
5	500	20	5	0.326
6	500	20	15	0.575
7	500	30	5	0.426
8	500	30	15	0.783

From an optimization perspective, the day's work is done; we can use run 8's parameters and be finished with the matter. However, with some statistical finesse, we can get more information from this data.

1.3 Ranking and Significance of Factors

Suppose we wanted to rank the factors in order of their effect on X_A. A simple procedure, termed the column effects method, can do this easily [3]. The procedure is:

i. Choose a factor and a level. Take the average of each measurement over all treatments which contain the chosen factor-level pair. For example, if we chose P = 20 bar, we would take the average of X_A for runs 1, 2, 5, and 6 in table 2, since these treatments all used P = 20 bar.
ii. This process is repeated for factor-level combination, forming a table.
iii. Subtract the least value in each row from the largest. The size of the resulting differences rank the factors by the strength of their effect on the test subject.

The column effects analysis for the reactor experiment is shown in table 3 below:

Table 3: Column effects analysis of table 2.

		Level Averages		
		1	**2**	**Max-min**
Factors	**T (K)**	0.317	0.527	0.211
	P (bar)	0.360	0.484	0.123
	F_A (mol/min)	0.301	0.543	0.243

From the results in table 3, we conclude that the ranking of the factors by their strength of their effect on X_A is F_A > T >> P.

Readers familiar with statistics are likely wondering, "How would one know if these differences are statistically significant?" This is a drawback to this approach; statistical significance cannot be ascertained; only relative rankings. A further drawback is that the significance of interaction effects cannot be estimated. An interaction effect is an effect that is a function of the levels of two or more factors. In simple terms, it is a synergistic effect between variables that produces a "whole greater than the sum of its parts."

The analysis of variance (ANOVA) method however, can tell which factors and interactions are statistically significant. The column effects method is actually a simplified version of ANOVA [3]. Unfortunately, the general procedure for multivariate ("n-way") ANOVA is very complicated, and the chance of miscalculation is high when done by hand. For brevity, we refer the reader to the appendix for a 2-way ANOVA example.

Despite the complexity of n-way ANOVA, modern scientific computing software can do the operation swiftly. Table 4 below shows the ANOVA, calculated in MATLAB, of table 2:

Table 4: ANOVA for the plug flow reactor scenario.

Factor	Sum of Squares	df	Mean Square	F	p-value (%)
T	0.08883	1	0.0888	384.34	3.2445
P	0.03038	1	0.0304	131.45	5.5387
F_A	0.11737	1	0.1174	507.82	2.8232
T × P	0.00189	1	0.0019	8.18	21.4100
T × F_A	0.00738	1	0.0074	31.94	11.1500
P × F_A	0.00374	1	0.0037	16.19	15.5090
Error	0.00023	1	0.2498		
Total	0.24983	7			

A factor is significant if its p-value is less than the significance level, α, which is typically 5-10%. If α = 5%, we conclude that T and F_A are significant factors, and that there are no statistically significant interaction effects. Since there was only one observation per treatment, the error was approximated using the three-way T × P × F_A interaction.

1.4 Full Factorial Designs

The experimental design used in §1.2 was a full-factorial design (FFD), so-named because every factor-level combination was tested. FFD's convey more information than any other design [2]. If at least 2 observations are taken for each run, a FFD is capable of testing the significance of all main effects and interactions. Otherwise, the highest-order interaction is approximated as the error term in the ANOVA.

However, FFD's are rarely used in practice, since they require large numbers of runs. This is especially true in catalyst synthesis. Consider a relatively tame 4-factor, 3-level experiment. A FFD experiment would need $2 \times 3^4 = 162$ observations, an infeasible number. Due to the "combinatoric explosion" that FFD's suffer from, it is common in scientific and industrial practice is to use fractional-factorial experiments (FFE).

1.5 Fractional Factorial Designs and Orthogonal Arrays

Despite conveying less total information, FFE's can capture much of the variation in the data with fewer runs. The justification for using

FFE's is based on the sparsity of effects principle, which states that the effects of higher-order interactions, though ubiquitous, are usually insignificant [4].

Orthogonal arrays (OA's) are a type of FFE that can test the significance of many factors with few runs. Also known as Taguchi arrays, OA's are widely used in industry and research when confronted with situations where the number of experimental factors is intractable. They are especially common in manufacturing, medicine, and agriculture [4].

The origin of OA's can be traced back to 19th-century French mathematician Jacques Hademard [3], but they were forgotten until World War II. OA's received heavy attention in post-war Japan. Since Japan is an import-dependent island nation, raw materials are scarce and expensive. Manufacturers were reluctant to spend money and resources on experimentation without a definite payoff. OA's vastly reduced the cost of industrial experimentation, which was instrumental in Japan's post-war industrial comeback. By greatly reducing the cost of experimentation, Japanese industry was eventually able to produce Western-quality goods.

At first glance, it is not obvious what exactly is "orthogonal" about these arrays. The orthogonality of these arrays relates to their statistical properties, and is unrelated to the vectorial definition of orthogonality. The statistical definition of orthogonal means "zero correlation." Two variables are said to be "orthogonal" if they are uncorrelated (e.g. Pearson-squared = 0.)

OA's fit nicely into sequential experimentation strategies. Consider a researcher investigating an 8-factor system. Suppose the results of a OA experiment judges 2 factors as significant. With only 2 significant factors, the scope of the experiment can be vastly reduced. The researcher could then do a FFD experiment on the two significant variables to see if there is an interaction effect between them, and set the other 6 variables to whatever is most convenient. Using the FDD first would have likely driven the researcher mad, but this sequential strategy has saved him much time and effort.

To understand what it is that makes orthogonal arrays "orthogonal", we introduce the concept of a statistical contrast. For analyzing multi-factor experiments, a commonly used statistic is a contrast. A contrast, C, is any linear sum of cell means, μ_i, with coefficients, c_i, that sum to zero:

$$C = \sum_i c_i \mu_i \qquad (1)$$

$$\sum_i c_i = 0 \tag{2}$$

Two contrasts are orthogonal if:

$$c^T c = 0 \tag{3}$$

Contrasts are a generalization of the differences between level means used in column-effects analysis, as discussed in §1.3. In column-effects analysis, only differences between main effects are calculated, while the generalization with contrasts allows the measurement of interaction effects.

Statistical orthogonality indicates that there is no correlation between the contrasts, which is highly desirable. Since there is no correlation, the contrasts convey completely different information about the experiment. This is the origin of the term "orthogonal array" – the contrasts (and other statistics) that are estimated from OA's are uncorrelated, and thus are a more efficient at obtaining information via experiment.

A drawback of OA's is that no arbitrary OA will fit any arbitrary factor-level set. The experimenter must adjust his experiment to match the OA that best suits his needs. Also, OA's are not readily obvious; they must be found using either published lists of designs [5], or computer programs. Also, the levels of the chosen OA must be evenly spaced.

1.6 Definition and Properties of Orthogonal Arrays

We begin with a formal definition [4]:

An N × k matrix is a OA if all N × t sub-matrices of M contain all s^k level combinations, repeated λ times each.

Any given orthogonal array, designated by $OA_\lambda(N,k,s,t)$, has N runs, k factors, s levels, strength t, and index λ. For example, consider the OA below with t = 3.

Table 5: The OA(9,4,2,3) array.

1	0	0	0
0	1	0	0
0	0	1	0
0	0	0	1
0	1	1	1
1	0	1	1
1	1	0	1
1	1	1	0

There are 2^3 possible level combinations for 0 and 1, which are: 000, 001, 010, 100, 011, 101, 110, and 111.

Observe the submatrix created by columns 1, 2, and 3 of the OA above:

Table 6: Submatrix of columns 1, 2, and 3 of Table 5.

1	0	0
0	1	0
0	0	1
0	0	0
0	1	1
1	0	1
1	1	0
1	1	1

From the above definition, we see that this array is correctly designated as $OA_1(8,4,2,3,1)$. We see that each combination appears exactly once, and thus $\lambda = 1$. The same is true for the submatrices created by concatenating columns 1-2-4, 1-3-4, and 2-3-4. Though the example given above has $\lambda = 1$, λ can be greater. An example is the $OA_2(8,5,2,2)$ array [5]:

Table 7: The OA(8,5,2,2) array.

0	0	0	0	0
0	0	1	1	1
0	1	0	1	0
0	1	1	0	1
1	0	0	1	1
1	0	1	0	0
1	1	0	0	1
1	1	1	1	0

Higher strength is a desirable property of a OA, since more level combinations are used. However, this also makes the array more difficult to create, and thus the strength is usually capped at 4 [5].

1.7 Use in Photocatalytic Research

The synthesis of photocatalytic semiconductors is often a multi-step process, with several "tweak-able" factors at each step. Examples from the literature include sol-gel methods [6-9] and amorphous precursor methods [10-12]. FFE designs are an excellent way of finding the important factors in the synthesis of the catalyst, and/or for optimization. Despite the advantages of FFE's, most of the literature has used the "one-variable-at-a-time" method, or some variation thereof. To the best of our knowledge, the first use of orthogonal arrays in photocatalytic research was done by Zhao et al. in 2009 [9].

In this work, we have used a OA design [13], $OA_1(9,4,3,2)$, to maximize the rate constant of the photocatalytic degradation of an organic dye pollutant, methyl orange. The array is shown below:

Table 8: The OA(9,4,3,2) array.

0	0	0	0
0	1	1	2
0	2	2	1
1	0	1	1
1	1	2	0
1	2	0	2
2	0	2	2
2	1	0	1
2	2	1	0

The factors manipulated were $InVO_4$ concentration, nickel concentration, $InVO_4$ calcination temperature, and ball-milling time. Interactions were not considered in this study. An FFD for this system would have needed $3^4 = 81$ experiments, while the above OA requires 9. An in-depth explanation of the choice of factors is given in §4.4.

Chapter 2: Semiconductor Physics

In this chapter, we introduce the concept of the semiconductor band gap, methods for altering it, and the important charge transfer processes that occur in semiconductors. Lastly, we examine how band gaps are typically measured. This brief treatment should prepare the reader well enough to understand this work. There are however, many excellent, comprehensive references on the subject, such as Kittel [14] and Beam [15].

2.1 Band Gaps

In the quantum mechanical theory, electrons in solids occupy discrete energy levels. At the ground (low-energy) state, electrons are locally bound to their respective atoms, and do not travel through the bulk of the solid. This set of low-energy electronic states is termed the valence band. If an electron is energized sufficiently, it can leave the valence band and freely conduct throughout the solid. This set of high-energy states is termed the conduction band, and the amount of energy required to reach it is termed the band gap (E_g, in electron-volts). "Wide band-gap" semiconductors (E_g > 2.2 eV) have found many applications in scientific and industrial use [16].

Figure 2 below illustrates photon absorption. In the figure, a valence band electron (e_{vb}) absorbs light with energy hv > E_g, and then jumps to the conduction band. This creates a free-roaming pair of charge carriers – a conduction band electron (e_{cb}^-) and a valence band hole (h_{vb}^+). These charge carriers, e_{cb}^- and h_{vb}^+, are of fundamental importance in semiconductor physics and photocatalysis.

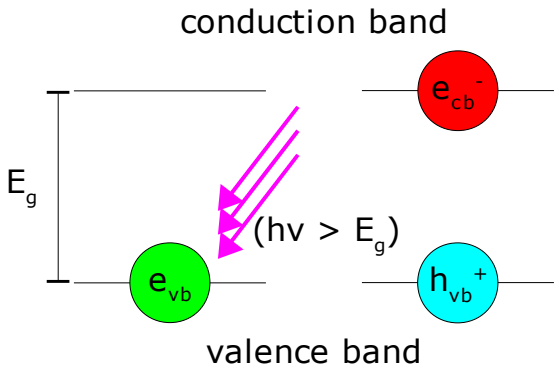

Figure 2: Photon absorption and charge carrier pair generation.

2.2 Band Theory

The formation of bands is a consequence of the greater number of atoms present in a solid body – the greater the number of atoms, the greater number of possible electronic states. Figure 3 below illustrates band formation with increasing atom population. As the number of atoms increases, the energy levels blur together into continuous bands.

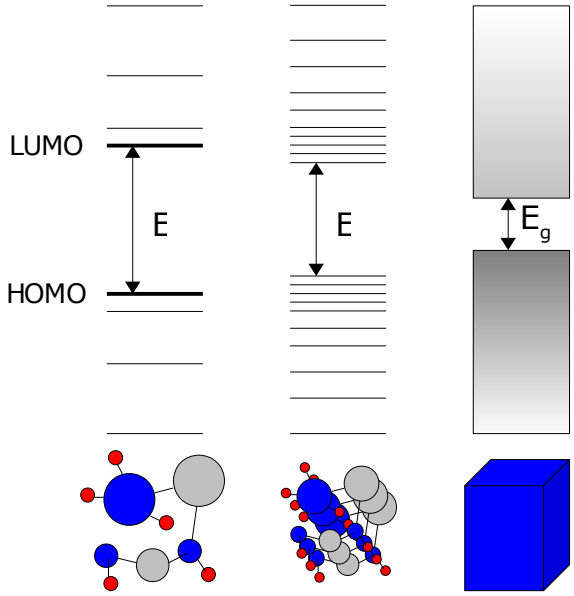

Figure 3: Formation of bands in a semiconductor.

The band gap widens as the number of atoms decreases. This behavior, broadly termed "quantum-size" or "quantum dot effects", results from the lower number of available energy states.

2.3 Insulators, Metals, and Semiconductors

Figure 4 below gives shows band structures for the three main classes of electrical materials: insulators, semiconductors, and metals.

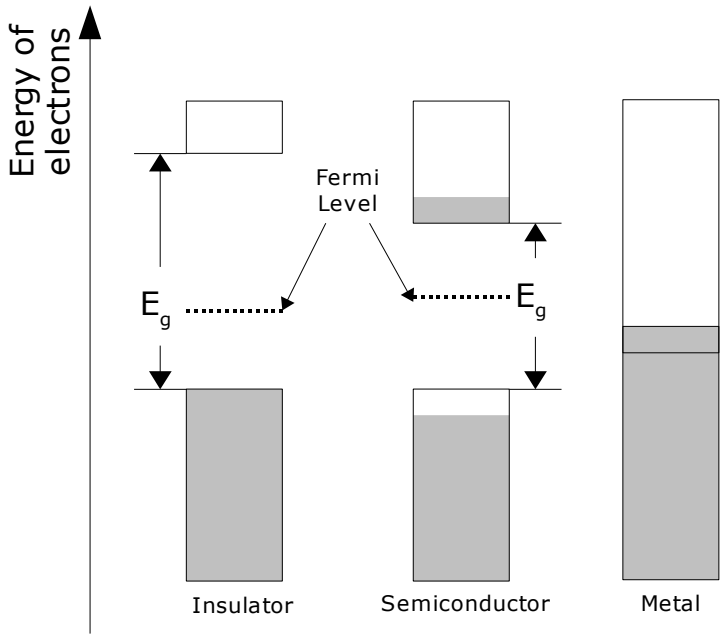

Figure 4: Insulators, semiconductors, and metals.

Due to the large band gaps in insulators, the valence band is full and the conduction band is empty. Since electrons have great difficulty entering the conduction band, the electron mobility in insulators is extremely low. Thus, current flow through insulators is practically zero. Metals conduct by default; the conduction and valence bands overlap, and thus, there are always free electrons available for conduction. This is due to how loosely-bound the valence electrons are in metals. This loose-binding which results in an "electron sea" surrounding the atomic nuclei in the material, facilitating free transport of electrons throughout the solid.

In semiconductors, the band gap is small enough to be traversed when an electron becomes sufficiently energized, but is still large enough to hinder conduction. This unique property makes

semiconductors useful for many applications, such as circuit elements, computer chips, chemical catalysts, and photovoltaic devices. Altering the physical properties of semiconductors allows alteration of the width of the gap, as well as the position of the band edges.

2.4 Defects and Chemical Doping

The band structures in figure 4 only hold true in an infinitely periodic medium. In reality, no medium is ever perfectly periodic, due to the existence of structural defects. The electronic properties of semiconductors can be altered by the addition of defects into the crystal structure of the material. A common technique for introducing such defects is doping, where another element is substituted for another atom in the crystal lattice. Even trace amounts of dopant can drastically affect the electrical and optical properties of semiconductors [14].

There are two kinds of doping, shown in figure 5 below. In the left of the figure, all carbon atoms in the undoped diamond lattice are bonded to each other covalently, and there are no local charge imbalances. The forbidden zone and conduction bands are both empty. In the middle of the figure, we have doped the diamond with nitrogen. Nitrogen is pentavalent, while carbon is tetravalent, and thus, nitrogen will add an extra electron (green circle) to the lattice. This extra electron can easily conduct through the solid. This is known as n-type doping, since the extra electrons create a negative charge (the reader is advised that the "n" in this sense has nothing to do with the elemental symbol "N" for nitrogen.) This doping creates permissible electron-donating states within the forbidden zone, near the conduction band edge (figure 5 middle).

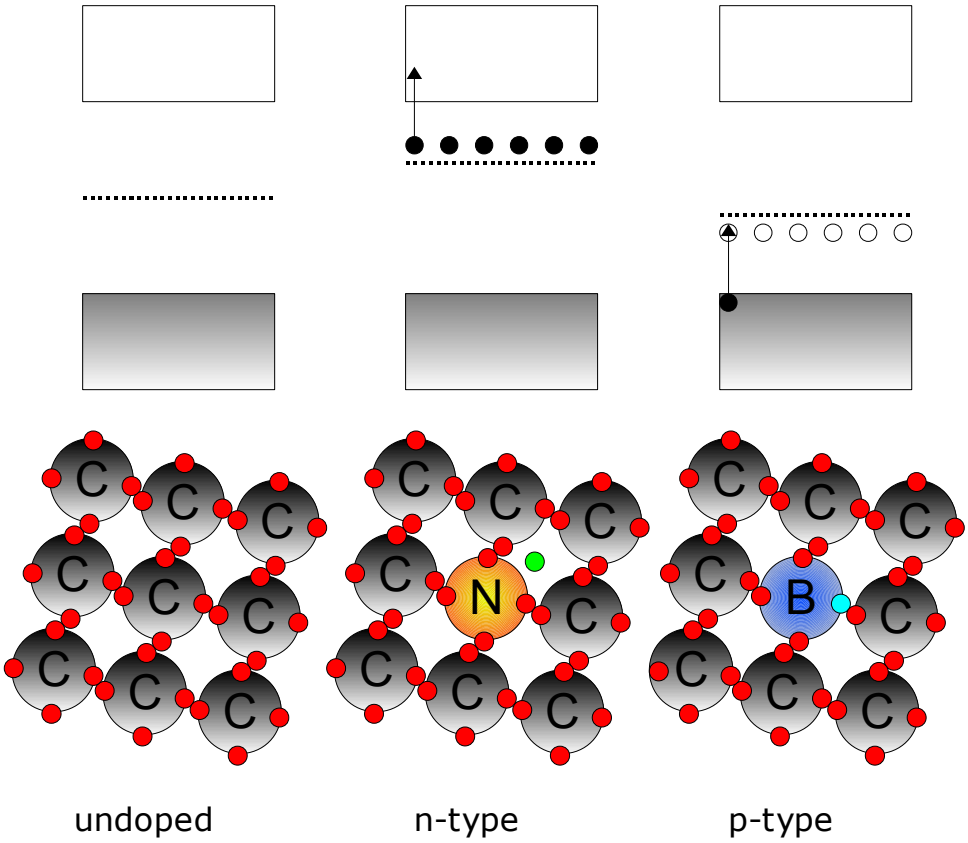

Figure 5: Undoped, n-type, and p-type diamond.

p-type doping is the opposite; we instead dope with an element that is electron-deficient compared to the bulk material. In the right of figure 5, we have doped with trivalent boron. To satisfy the octet rule, boron will steal a nearby carbon-bound electron. This continuous thievery of electrons from neighboring atoms results in the conduction of h_{vb}^{+} through the medium. In the band structure of the p-doped diamond, electron-accepting states have been created near the valence band. In both cases, the Fermi level (dotted line) is dragged towards the energy states created by the dopants [17].

Structural defects, such as vacancies, dislocations, and the surface of the solid can also affect the electrical properties of a material [18]. Defects introduce permissible energy levels into the forbidden band, just like dopants. There are many ways of introducing defects into solids, such as ion bombardment [15] and high-energy ball milling. Generally, the strength of a given defect is determined by its size – point defects only affect one atom, while dislocations affect lines of atoms, and a surface (or stacking fault) affects a plane of

atoms [15]. Defect states are especially important in the process of trapping and recombination[15,19], and are discussed in §2.5.

2.5 Generation, Recombination and Trapping

Free electrons are "generated" when an e_{vb} jumps from the valence band to a forbidden-zone defect state or the conduction band. There are two ways in which this can occur. Thermally-generated lattice vibrations, known as phonons, can supply energy for the transition. Another way is for a photon, or quanta of light energy, to be absorbed by an electron.

When an e_{vb} jumps, two charge carriers are generated – an e_{cb}^- and a h_{vb}^+. These carriers randomly move through the solid until they become trapped or recombine. Figure 6 below illustrates these processes.

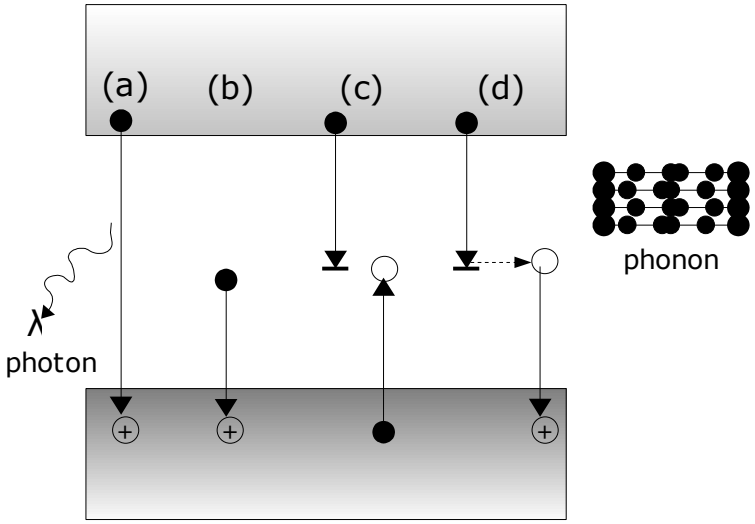

Figure 6: Various recombination modes in semiconductors.

Recombination occurs when an e_{cb}^- returns to the valence band. In path (6a), e_{cb}^- drops into the valence band directly from the conduction band, releasing a photon. This is known as radiative recombination. Radiative recombination is probabilistically unfavorable usually, and most e_{cb}^- recombine with h_{vb}^+ by dropping in from a lower-energy defect state (figure 6b).

Trapping occurs when an electron moves into a defect state near the center of the band gap (figure 6c). Shallowly-trapped electrons are held for $\sim 10^{-9}$ seconds , while deeply-trapped electrons can be held for

hours [15]. Figure 6d shows a special state configuration called a recombination center, where an e_{cb}^- filters through two or more defect states that aid in recombination. In general, phonons are released when an electron takes paths 6b-6d.

Recombination is highly undesirable in photocatalysts. High recombination rates result in low energy efficiency, since the photonic energy used to generate the e_{cb}^-/h_{vb}^+ pairs is wasted. By careful preparation of the semiconductor material, either by introducing defects or dopants, one can decrease the recombination rate.

2.6 Direct and Indirect Band Gaps

An important concept relating the photonic efficiency of semiconductors is the directness or indirectness of the band gap. Figure 7 below illustrates both types.

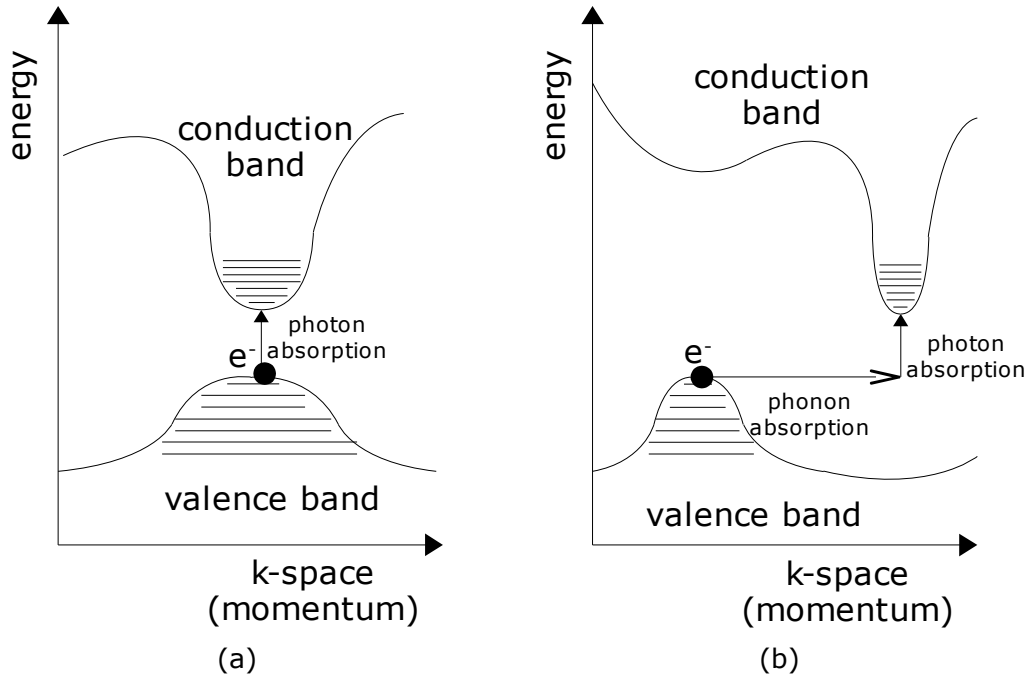

Figure 7: Direct (a) and indirect (b) semiconductors.

In a direct band gap semiconductor (figure 7a) the valence band maximum and conduction band minimum have equal crystal momenta, k. A detailed discussion of crystal momentum is beyond the scope of this work and the reader is referred to [14]. Once a photon is absorbed, e_{vb} jump to the conduction band.

In figure 7b, the valence and conduction band edges are separated by some large k. Photons have little momentum to transfer to the electron, which means that a photon alone cannot excite an e_{vb} to the conduction band [15]. Instead, a phonon must be absorbed to give the electron the required momentum, and then a photon must be absorbed to provide energy for the jump.

2.7 Measurement of the Band Gap

Accurate measurement of the optical band gap is done using spectroscopy techniques in the visible and UV ranges. The absorption spectra generally shows strong absorption in the lower wavelengths, which transitions to near zero at long wavelengths. This transition, termed an absorption edge is a function of the optical band gap [20]. For transparent films, transmittance spectroscopy can find the band gap. For opaque specimens or powders, diffuse-reflectance spectroscopy (UV-Vis DRS) is used. To find the band gap, a tangent line is drawn through the absorption edge, and its intersection with the abscissa (wavelength) is found. This wavelength corresponds to the optical band gap. Figure 8 below shows a characteristic absorption edge. To convert the reading of E_g to electron-volts, take 1240/λ, where λ is the wavelength in nanometers.

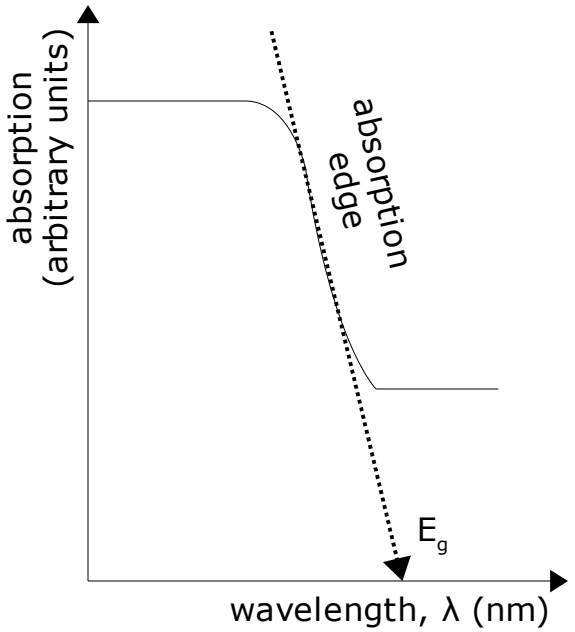

Figure 8: Absorption edge and the optical band gap.

Chapter 3: Background on Photocatalysis

This chapter reviews heterogeneous photocatalysis as it relates to water detoxification. We discuss the general mechanism for the photocatalytic formation of reactive oxygen species (ROS), and the role these species play in the photo-degradation of pollutants. Important factors affecting kinetics are also discussed.

3.1 Photocatalysis for Water Purification

Contaminated industrial wastewater is a major environmental problem. Dyes and other wastewater runoff from textile industries are difficult pollutants to treat. Discharge of this wastewater into the environment causes eutrophication of natural water sources and aesthetic pollution [21,22]. The primary degradation products of these dyes are aromatic amines, which are typically carcinogenic [21]. Most current treatment methods, such as activated carbon and reverse osmosis, merely concentrate the pollutant into another phase, without destroying it [21-23]. Other methods, such as chlorination and ozonation, can destroy the dye but are costly and/or energy-intensive [22].

Semiconductor photocatalysts use photonic energy to mineralize organic pollutants into inert CO_2 [24]. Photocatalysis is especially attractive for organic pollutant disposal, since many toxic organics contain highly-conjugated aromatic systems, which are resistant to chemical attack. Such aromatic systems however, are preferentially attacked by the reactive oxygen species produced during photocatalysis [25]. Photocatalysis offers an energy-efficient and more-effective means of water remediation. These potential benefits have made the development of reactive photocatalysts a major effort in green chemistry.

Besides oxidation reactions, photocatalysts can reduce chemicals as well, such as CO_2 and toxic heavy metals [24,26]. The prospect of using visible-light solar energy to reduce CO_2 into automotive fuels, such as methanol, is particularly appealing. Similarly, many photocatalysts have been experimented with for water-splitting as a

means of producing hydrogen. However, little success has been achieved for this purpose under visible light, and more work remains.

3.2 General Mechanism of Photocatalysis

The basic mechanism of photocatalysis, adapted from [27], consists of 5 general steps, shown in figure 9 below.

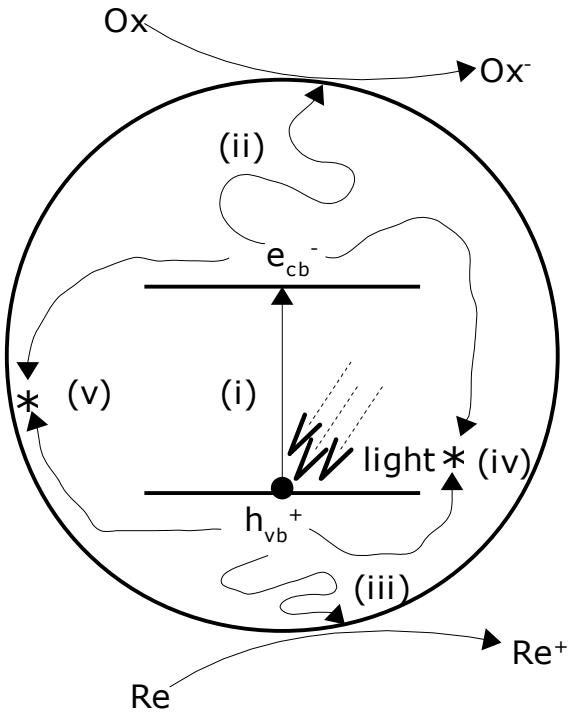

Figure 9: Charge carrier paths in a catalyst particle.

The most straight-forward reaction pathway is:

i. Excitation of e_{vb} into the conduction band by light with hv ≥ Eg, produces e_{cb}^- and h_{vb}^+.
ii. e_{cb}^- migrates to the surface, where it reduces the oxidizing species, Ox.
iii. h_{vb}^+ migrates to the surface, where it oxidizes the reducing species, Re.
iv. Recombination of a charge carrier pair in the bulk volume of the particle.
v. Recombination of a charge carrier pair in a surface state.

Path (v) becomes important at low particle sizes, when the ratio of surface area-to-volume is large, and surface defect states are relatively more common [23].

For organic pollutants, the mechanism is slightly longer. The oxidizing species in this case, is dissolved oxygen, O_2, which is reduced to the superoxide anion, O_2^-, and the reducing species is a hydroxyl anion, OH^-, which is oxidized into a hydroxyl radical, $OH^\bullet$. The hydroxyl radical then attacks adsorbed pollutant molecules on the surface. $OH^\bullet$ are potent oxidizing agents, outdoing ozone by a factor of $\sim 10^8$ [24]. The end product of the reaction depends on the reactant composition(s) and the amount of time allotted for photoreaction. Carbon atoms eventually oxidize completely to CO_2, nitrogen atoms to NO_3^-, and sulfur atoms to SO_4^{2-} [22,26].

The Langmuir-Hinshelwood rate law tends to fit the behavior of aqueous photocatalytic degradations [22,26,28,25]:

$$r = k\left(\frac{KC}{1+KC}\right) \tag{4}$$

Where r is the reaction rate, k is the reaction rate constant, K is an adsorption constant, and C is the reactant concentration. When $C >> 1$, the rate law reduces to zero-order ($r = k$), and when $C << 1$, it reduces to first-order ($r = kKC = k_{apparent}C$).

3.3 Factors Affecting Photocatalytic Reaction Kinetics

i. Wavelength and Intensity: Short wavelengths of light are more effective at degrading organics, presumably because of their greater energy. Wavelengths of light with $hv < E_g$ do not excite the photocatalyst, and thus no reaction occurs. At low light intensities, the effect on rate is linear, but transitions to a square-root dependence at higher intensities. This is generally attributed to greater recombination [26].

ii. Temperature: At the lower temperature extreme, the desorption of products from the catalyst surface is unfavorable, hindering the degradation. At high temperatures, adsorption of the dye is hindered. In between these two extremes, little effect is seen on the degradation. Generally, room temperature is the standard operating condition [25].

iii. Initial Concentration and Catalyst Mass: Catalyst concentration in the reaction slurry affects the rate linearly at lower concentrations,

and then saturates. This is due to obstruction of the the light source by other catalyst particles. The effect of initial reactant concentration is similar. For a given mass of catalyst, there are a finite number of sites for adsorption. When enough reactant is added to occupy all available sites, further addition of reactant is inconsequential. This is supported by the Langmuir-Hinshelwood behavior of the kinetics.
iv. pH: In colloidal dispersions, the pH is one factor that determines the level of agglomeration. Greater agglomeration means less surface area, and thus, a lower reaction rate. The pH also changes the surface charge of the particles and/or the charge of the reactants, which can affect the adsorption behavior of the system.

3.4 Titania (TiO_2), P-25, and $InVO_4$

Titania (TiO_2) has several desirable properties that have made it the "gold standard" photocatalyst for treating organic pollutants [24,26,27,29]. Titania is inexpensive and chemically-inert, unlike metal sulfide-type photocatalysts [26]. However, TiO_2 has poor activity in the visible-range due to its wide band gap (E_g) of ≈3.2 eV, which lies in the near-UV. The three phases of TiO_2, anatase, rutile, and brookite, are shown in figure 10 below [30-32].

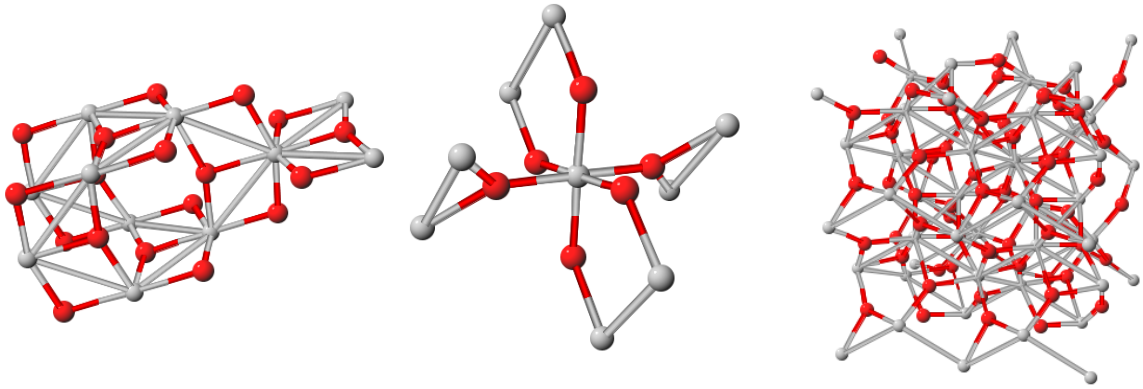

(a) (b) (c)

Figure 10: (a) anatase, (b) rutile, (c), brookite.

Anatase and brookite are low-temperature forms of TiO_2, which transition to rutile at ~600 °C and ~700 °C, respectively [33]. Anatase has been shown experimentally to be the most photocatalytically-active lone phase of TiO_2 [23], though mixtures of the phases have

shown superior results. The mixture used in this work was Degussa P-25, which is a mixture of ~3:1 anatase:rutile. Most photocatalysis research has focused on the alteration of the band gap and/or charge-separation of TiO_2 and P-25, either by doping, coupling with other metal oxides, and/or exploitation of quantum size effects.

Indium vanadate ($InVO_4$) is another photocatalyst with $E_g \approx 1.8$-2.0 eV. It has been demonstrated to split water and reduce CO_2 into methanol, both under visible light [34-37,11]. The structure of $InVO_4$ is temperature-dependent. We are concerned primarily in this work with the orthorhombic high temperature phase, $InVO_4$-III. The reader is referred to the literature for the structure [34,35].

In this work, we have explored the use of a combined P-25/$InVO_4$ photocatalyst, doped with nickel. Coupling of semiconductors with mismatching E_g can lead to better charge separation. This is thought to occur by first exciting e_{vb} in the oxide with the lower E_g [6]. The generated e_{cb}^- then migrate into another oxide, whose conduction band is positioned lower (energy-wise) relative to these e_{cb}^-'s current position. Due to this transfer of charge, there will be a preponderance of e_{cb}^- in the wider-E_g semiconductor. In this way, the e_{cb}^--h_{vb}^+ recombination rate is diminished by better separation of the charge carriers. To explore this idea further, we present a band edge diagram for TiO_2 and $InVO_4$ in figure 11 below [6,23,26,37,38]:

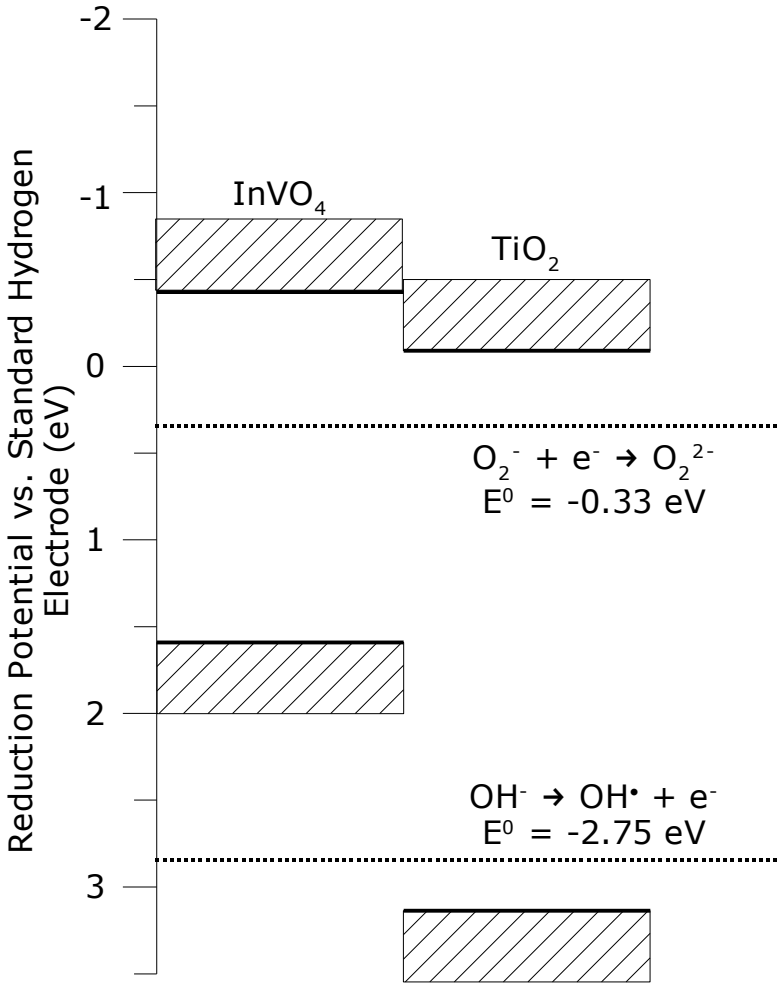

Figure 11: Band edge diagram of $InVO_4$ and TiO_2.

In the figure above, $InVO_4$ has its conduction band positioned above TiO_2's. $InVO_4$'s valence band is positioned above the oxidation potential for the hydroxide ion, and thus, hydroxyl radicals cannot be formed with $InVO_4$. The purpose of coupling $InVO_4$ and TiO_2 is to exploit the higher conduction band of $InVO_4$ as a way to separate charge. If electrons are sequestered in the $InVO_4$, they cannot recombine with h_{vb}^+ in TiO_2.

Chapter 4: Experimental Procedure

The goal of this study was to maximize the degradation rate constant of our model pollutant, methyl orange dye (MO), by manipulating key variables in the photocatalyst synthesis: the weight fraction of $InVO_4$ (w_{InVO4}), the weight fraction of Ni (w_{Ni}), the calcination temperature of $InVO_4$ (T_{calc}, °C), and the milling time (t_{mill}, hr). An orthogonal array experimental design was used to investigate these factors. We also discuss the techniques used in the catalyst synthesis, such as the organic precursor calcination technique, ball-milling, and a discussion of the important experimental variables.

4.1 General Outline of Procedure

A major challenge in this study was the large number of possible experimental variables in the synthesis. A OA design was used to keep the number of required experiments at a reasonable number, while not requiring us to discard too many important variables from investigation. OA's have been applied to semiconductor photocatalysis previously [9]. Interactions were not tested. The 9-level orthogonal array is shown in table 9 below:

Table 9: OA9 orthogonal array design.

Run #	w_{In} (%)	w_{Ni} (%)	T_{calc} (°C)	t_{mill} (hr)
1	1	1	600	4
2	1	2	700	12
3	1	3	800	8
4	2	1	700	8
5	2	2	800	4
6	2	3	600	12
7	3	1	800	12
8	3	2	600	8
9	3	3	700	4

After measuring the kinetics of these 9 samples, the results were used to estimate which factor-level combinations would produce the two catalysts with the fastest and slowest reactivity. These catalyst samples were synthesized and also tested in the reactor. We then characterized the two samples out of the entire set of 11 that were the slowest and fastest, to see which physical properties most strongly affected the reactivity.

4.2 Background on OPC Synthesis Procedure

A common technique for making photocatalysts is the solid-state reaction method [34], where pressed reactant powders are calcined. Though simple and widely used for creating metal oxides, it has several disadvantages. The temperatures used are high, usually 1000 °C+. Also, the final product is typically inhomogeneous, due to poor reaction-diffusion kinetics in the solid phase [11]. Lastly, the product generally has a low specific surface area, requiring subsequent comminution to increase reactivity. Another synthesis technique, termed in this work as organic precursor calcination (OPC), has none of these drawbacks.

OPC is used for the production of supported and unsupported catalysts, especially metal oxides. The procedure involves reacting a heated, aqueous solution of metal oxide or metal ion with a multidentate ligand to create an amorphous precursor. A ligand is any large molecule with multiple Lewis base sites on it that can attach to a metal atom [12]. "Multidentate" means "many-toothed", and refers to the number of available base sites. Good ligand choices for OPC are organic acid salts of citric, malic, tartaric, glycollic, or lactic acid [12]. A typical ligand:metal ratio is one mole of the carboxylic acid functional group per mole of metal atoms [10]. This procedure has been used to produce highly-dispersed supported metal catalysts and metal oxide catalysts. OPC was used in this work to synthesize $InVO_4$, a component of the photocatalyst.

After the metal-ligand reaction is done, the precursor solution is dried overnight under heat and possibly vacuum [10]. The solution viscosity increases greatly as water is removed. The addition of poly-alcohols, like ethylene glycol, can also increase the viscosity via a polyesterification reaction. The "final precursor" is a solid, amorphous foam or transparent glass. The amorphous precursor is then calcined to ablate the organics, producing the final product. Calcination temperatures are usually 600 °C or greater [10]. Typical calcination atmospheres are air or O_2 [10]. Decomposition of the precursor usually

produces CO, CO_2, H_2O, and/or NO_x gases [10]. The typical particle size range for the produced oxides is 30 - 5000 Å, with higher temperatures yielding larger particles [10].

4.3 Background on Ball-Milling

High-energy ball-milling (HEBM) is a powder-processing technique in which the sample is pulverized by hard, solid balls. The method was first put to industrial use in the 1960's for the production of advanced materials for the aerospace industry [39]. Since then, HEBM has found further use in microelectronics, manufacturing, medicine, and the military [40,39]. A comprehensive review of the subject has been given by Suryanarayana [41].

The basic operation of the mill is simple to understand. First, the balls and powder are loaded into a stout, cylindrical vial. This vial is then secured within a rotating "sun-wheel" apparatus, which rotates at high-speed, causing the crushing action. Typically, the vial and disk rotate in opposite directions. Typical milling media are stainless steel, agate, and ceramic. The vial and balls are usually made from the same material. Many factors affect the final product [39], such as the powder-to-ball mass ratio, the temperature, powder composition, milling atmosphere, size and shape of the powder particles, the milling time, the composition and shape of the milling media, and the amount of and type of process control agent. Process control agents are gummy materials, such as stearic acid, that inhibit cold-welding [39].

HEBM, though simple in concept and execution, is a complicated stochastic process. Powders can be milled dry, or with a liquid dispersant such as water or alcohol. Dispersants also hinder cold-welding, since the wetting action of the dispersant stabilizes particle surfaces, thus hindering cold welding. Figure 12 below, based on that given by [42], gives an idealized setup of activity in the mill.

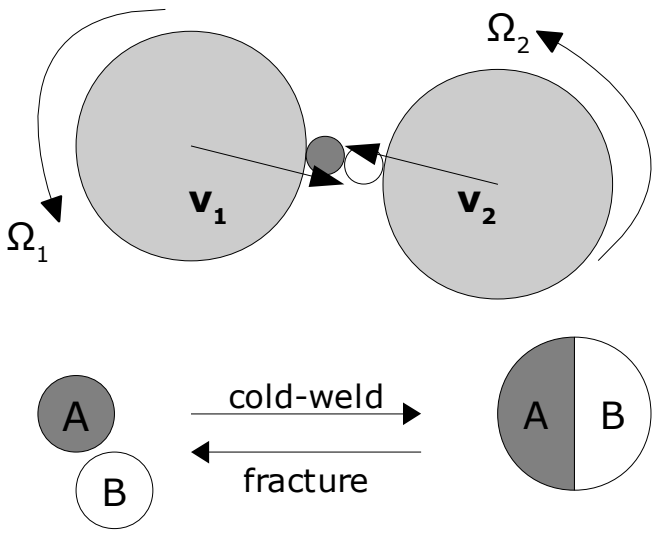

Figure 12: Activity inside a ball mill.

Each ball has translational velocity v_i, and angular velocity Ω_i. Powder particles A and B, which are not necessarily of different composition, line up in the path of two balls, and a collision results. The particles are subjected to a severe shock impulse, causing them to cold-weld or fracture. The probability of either outcome is dependent upon v_i, Ω_i, and a host of other factors. Computational simulations have had limited success in predicting the material properties of the of the mill products from a set of input variables [39]. Discrete element method simulations by Mio et al however, have suggested that asymmetric rotation of the disk and vial is most effective for grinding [43].

The attrition of the powder particles follows three general steps, as given by Le Caer [42]:

i. Mixing and plastic deformation of the components, which produces a cold-worked composite with a lamellar structure.
ii. Equilibrium shifts towards cold-welding, which causes the lamellar structure to become progressively finer.
iii. Steady-state is reached between the welding and fracture processes, causing the particle size to reach equilibrium.

XRD results by Indris et al [44] show average grain size vs. time for several different powders, which demonstrates the aforementioned saturation behavior. Besides the lamellar structure, other defects are

also produced, especially grain boundaries. Suryanarayana presents SEM images of the lamellar structure [41]. The milling also increases the specific surface area of the powder via particle size reduction [40].

The major use of HEBM is to alter the physical properties of powders via the introduction of structural defects. Defects are produced during milling from the intense stresses exerted upon the powder grains during collision. Typical particle sizes of milled powders are < 1 μm, though grain sizes are much smaller, usually ~10 nm [39]. The technique has been used to produce non-equilibrium phases of solids, immiscible alloys, and solid solutions. It has also been observed to trigger chemical reactions. Displacement reactions, such as CuO + Ca → Cu + CaO, have been activated with HEBM at far lower temperatures than would normally be required [39]. This is why the method is sometimes referred as "mechano-chemical processing" [40].

Semiconductor powders can be easily doped via HEBM. Typically, the elemental metal powder is loaded in with the sample, and milled normally. Nonmetals, such as nitrogen, have also been doped into semiconductors using ball-milling.

There are several drawbacks to HEBM however. The milling media can self-grind during the process, introducing small amounts of contaminant into the powder. Metal media are often the most susceptible to contamination. The most effective ways of lowering contamination, as given by Suryanarayana [39] are:

i. Use of high-purity materials.
ii. Using the same material for the balls and vial.
iii. Coating the balls with the milled material.
iv. Short milling times.

In addition to contamination, it is difficult to form the milled powder into solid shapes, since this tends to remove the useful defects in the particle microstructure. HEBM scale-up is also expensive, which is why it has found relatively little use in industry [40].

Ball-milling has been used previously in photocatalytic research. Most investigators have focused on doping TiO_2 with metals, or coupling them with oxides. Moderate success with mechanically-milled TiO_2/SnO_2 has been reported in the literature, as well as doped Ni-TiO_2 [45,46] In photocatalysis, dopants and/or structural defects form electronic "trapping centers" for electrons, which aid in charge separation, and thus reduce the recombination rate [47].

4.4 Discussion of Chosen Experimental Variables

Many factors affect the reactivity of photocatalysts, such as defect concentration, crystal phase, and the photoreaction conditions. We narrowed our choices to variables related to the catalyst synthesis. The factors hypothesized to be most important in the synthesis were: the weight fraction of $InVO_4$ (w_{InVO4}), the weight fraction of Ni (w_{Ni}), the calcination temperature of $InVO_4$ (T_{calc}, °C), and the milling time (t_{mill}, hr).

i. Ni concentration: The amount of dopant(s) in a photocatalyst will affect the band structure, which influences reactivity. Low concentrations of dopant (1, 2, and 3 wt. %) were chosen. Doped transition-metal atoms act as charge carrier trapping centers. Trapping causes e_{cb}^- to be hindered during their random walk through the semiconductor lattice, which increases the probability that h_{vb}^+ will reach the surface and react with adsorbed surface compound(s). Too much dopant however, forms many recombination centers, and recombination will predominate over reaction [47]. Thus, an optimum doping level exists.
ii. $InVO_4$ concentration: $InVO_4$ cannot produce the hydroxyl radicals needed for photo-degradation, but it can help separate charge. Too little $InVO_4$ will reduce charge separation, and too much will slow the reaction due to a lack of TiO_2 active sites.
iii. $InVO_4$ calcination temperature: $InVO_4$ was synthesized by the OPC technique. For this synthesis route, calcination temperature is known to affect the amount of residual carbon content and the crystallinity of the resulting $InVO_4$ phase [11]. These factors could influence the charge separation and/or E_g of the photocatalyst.
iv. Ball-milling time: During ball-milling, the powder particles undergo severe plastic deformation by repeated collision with the balls and the interior of the milling vial. The longer the powders are milled, the more defect-rich their structure becomes. These defects can be effective charge separators. We suspect that longer milling time would be beneficial to the photoreaction due to greater particle size reduction, which would increase the specific surface area. However, too much milling would reduce the particle size so much that quantum dot behavior is observed, raising the band gap. Thus, an optimum exists between the specific surface area, particle size, and defect concentration.

4.5 Catalyst Synthesis Sub-Procedures

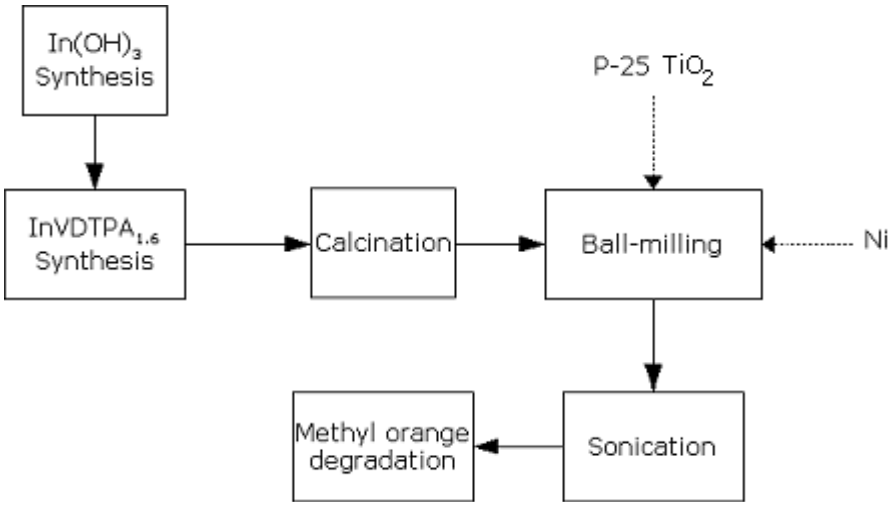

Figure 13: Flowchart of experimental procedure.

i. $In(OH)_3$ Synthesis: This method was used previously by Zhang et al [11], which was based on Szanics and Kakihana's method [48]. At standard conditions, indium oxide (In_2O_3) is water-insoluble. However, yellow In_2O_3 will dissolve in hot (≈85-90 °C), concentrated HCl, forming a clear solution. This appears to be from the formation of $InCl_3$, a soluble indium salt. The addition of excess base to the solution precipitated solid, white $In(OH)_3$ *(the reader is cautioned to add the base slowly during this step, or dangerous splashing of acid will result).* The precipitate is then recovered by any convenient means, e.g. vacuum filtration, sedimentation, or centrifugation.

The In_2O_3 used in this synthesis was purchased from Alfa Aesar, 99.9% metals basis. The HCl was aqueous 37 wt. %, and the base was aqueous NH_3 28 wt. %, both purchased from Sigma-Aldrich. 5 g of In_2O_3 was placed in a 1200 mL Pyrex fleaker with 25 mL of HCl and heated to 85 °C under vigorous stirring on a hot plate. A fume hood was positioned ≈5 inches above the mouth of the fleaker to vent noxious fumes. After the solution turned clear, 30 mL of aqueous NH_3 was slowly pipetted in 3 mL amounts into the fleaker. White $In(OH)_3$ crystals was formed immediately.

After the addition of the NH_3 was complete, the slurry was washed with 1000 mL of deionized H_2O. The $In(OH)_3$ particles were allowed to settle for about 30 minutes before being decanted. This washing step was repeated. After decantation the $In(OH)_3$ solids were

dried on a hot plate in a Pyrex petri dish under moderate heat. A distinct "cracked mud" pattern in the sample was a visual indicator of thorough drying. Yield of $In(OH)_3$ was typically >90%.

ii. $InVO_4$ synthesis: $InVO_4$ was formed by calcination of an amorphous, organic precursor, as described previously by [11,49]. Background information on the OPC method can be found in §4.2.

The precursor was made by reacting $In(OH)_3$ and V_2O_5 under heat with a multi-dentate ligand. The ligand used was diethylenetriaminepentaacetic acid (DTPA), purchased from Sigma-Aldrich, 98% pure. 5.5 g of DTPA were added to 50 mL of DI-H_2O and heated on a hot plate under vigorous stirring. After reaching 85-90 °C, 0.8 g of V_2O_5 and 1.45 g of $In(OH)_3$ were added. Gas bubbles evolved from the mixture, which eventually turned a royal blue color. This blue substance is suspected in the literature to be $InV(DTPA)_{1.6}$ [49]. The solution was dried on a hot plate heated to 150 °C.

After drying, the glassy blue precursor was powdered with a mortar and pestle, and spread out evenly on a refractory furnace tray for calcination. The powder was calcined at a ramp rate of 3 °C/min up to T_{calc}, and left to dwell at T_{calc} for a time length such that the total calcination time (ramp time + dwelling time) equaled 10 hours. The color of the calcined $InVO_4$ powder varied from light tan to dark brown, depending on the T_{calc} used. The $InVO_4$ was then left to cool to room temperature.

iii. Ball Milling Procedure: The $InVO_4$ was ball-milled with Aeroxide P-25 TiO_2 (Nippon Aerosil), and 99.9% Ni powder, 2.2-3.0 micron particle size (Alfa Aesar). All tools used for loading the vial, such as spatulas, graduated cylinders, and beakers, were washed with acetone before-hand, and dried in a 100 °C muffle furnace. Photographs of the Fritsch Pulverisette 6 ball mill and milling vial are shown in figure 14a below. Milling was done in a zirconia-alumina vial (figure 14b) with an inner diameter of 65 mm, and a volume of 83 mL. Fifteen zirconia-alumina balls (10 mm diameter) were used for the grinding. The ball:powder mass ratio was ≈10:1. 2.5 g total of powder was loaded into the vial with 5.0 mL methanol dispersant. The rotational speed was first brought up to 200 rpm for about 30 seconds, and then decreased to 150 rpm. The mill was set to reverse its rotational direction every 30 minutes. After milling was done, the vial was opened and dried for ≈10-15 minutes in an oven at 100 °C. The P-25's color was originally white, but turned light blue after milling with the nickel and $InVO_4$.

(a)

(b)

Figure 14: Photographs of (a) ball-mill and (b) milling vial.

High rotational speed was found to be ineffective. This was determined by listening to the mill. A rattling noise indicated that grinding was occurring, while no rattling indicated the balls were pinned down by high g-forces. This regime, termed "rolling" in the literature [43], is ineffective for grinding. The starting value of 200 rpm was used to get the balls moving inside the vial.

Though the literature reports that temperature can rise greatly during milling [42], this was not observed. The vial was touched immediately after milling ended. The was no noticeable difference from room temperature. The vial was thoroughly cleaned and dried after each run, and stored in a muffle furnace at 100 °C. The mill was supervised during the last 10-15 minutes of milling, to ensure that a power outage (or other unforeseeable event) did not interrupt the milling process.

4.6 Photocatalytic Reaction Procedure

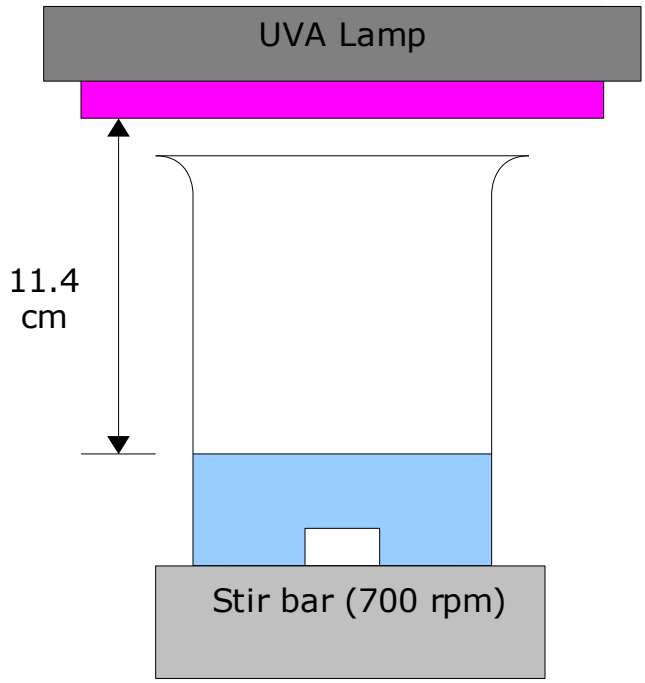

Figure 15: Batch slurry photocatalytic reactor.

The synthesized photocatalysts were tested in the batch slurry reactor (figure 15). It is practically identical to that used by [50], except no fume hood was used. A 500 mL Pyrex beaker was placed on a stir plate, with two 15-W UV-A (352 nm, spectrum available in [50]) lights positioned directly above the beaker. The UV intensity at the liquid surface was 2.1 mJ/cm^2, determined using a Chromaline UV Minder radiometer. The vertical distance from the air-slurry interface to the UV lights was ≈11 cm. 0.2 g of photocatalyst was placed in a 100 mL Pyrex beaker with 80 mL DI-H_2O, and sonicated for 1 hour for agglomeration. The catalyst dispersion was then added to a 500 mL Pyrex beaker, and then 1.7 mL of 600 ppm methyl orange (MO) solution was added using a Fisher Finnipipette pipette gun. Next, DI-H_2O was added until the solution volume was 200 mL. The resulting slurry composition was ≈5 ppm MO (mass basis), 1000 ppm catalyst. A low concentration of MO was used because photocatalysis closely fits 1st-order kinetics if the reactant concentration is low [26,29,25]. The dye was allowed to adsorb on the suspended catalyst particles for at least 1 hour in the dark under vigorous magnetic stirring. After adsorption, the first sample was withdrawn, which was used as the

initial absorbance (A_0). The beaker was then placed under the lights, and the stirring and lights activated. Due to absorption and light scattering, most of the reaction takes place in a thin "reaction zone" at the top of the liquid phase [50]. Because of this, fast stirring was used, and samples were withdrawn using a syringe from as close to the top of the air-liquid interface as possible. About 2 mL of sample was taken every 20 minutes, and stored in a microcentrifuge tip. Samples were stored in the dark to prevent ambient light from causing further degradation. As time progressed, the slurry color shifted from pale orange to milky white.

4.7 Characterization Procedures

i. Scanning Electron Microscopy (SEM): SEM sample stages and all tools were sonicated for 10 minutes in ethanol, and then 10 minutes in acetone. Double-sided silver tape was used for fixing the catalyst to the sample stages. Secondary-electron images were taken on a Hitachi S-800 SEM. The accelerating voltage was 25 kV, and the working distance was 5 mm.
ii. Energy-dispersive X-ray Spectroscopy (EDS): The Hitachi S-800 was equipped with an EDAX EDS detector. The sample was tilted at 30 degrees, which gave a take-off angle of 36.3 degrees. Silver tape was used to fix the powder samples in place. The ZAF correction was used. Unrealistic composition results were obtained at lower magnification, which is likely due to the electron beam being spread over a wide area. To remedy this, EDS spectra were taken at 10000x magnification, with an accelerating voltage of 25 kV.
iii. Brunauer-Emmett-Teller (BET) Surface Area Analysis: BET analysis was done using a Quantachrome Instruments Autosorb-1 Gas Sorption System with nitrogen gas. About 0.15 g of sample were used. Samples were outgassed for 24 hours before starting adsorption.
iv. Diffuse Reflectance Spectroscopy: Samples were pressed into compact pellets and analyzed using a OceanOptics DRS system. Barium sulfate was used as a standard. An integration time of 110 ms was used, and a 10-point boxcar method was used to smooth the data.
v. Methyl Orange UV-Vis Absorption Spectra: Prior to analysis, the liquid samples stored in the microcentrifuge tips were centrifuged in an Eppendorf 5415C centrifuge at 14000 rpm for 30 minutes. UV-vis spectra of the degraded dye samples were taken using a OceanOptics S2000 spectrometer, which used a DH-2000-BAL MikroPack halogen-deuterium lamp source. The arrangement was connected via USB to a

Dell Optiplex GX150 computer system. For each measurement, 750 ± 5 µL of liquid sample was placed into a disposable plastic cuvette using a Rainin digital pipette. An integration time of 5 milliseconds was used on the photodetector, and the data were smoothed using a 5-point boxcar method.

Chapter 5: Results and Discussion

5.1 Dye Degradation Results

Figure 16 visually shows the performance of the fastest catalyst (sample B), transitioning from orange to clear. This behavior is representative of the other catalysts.

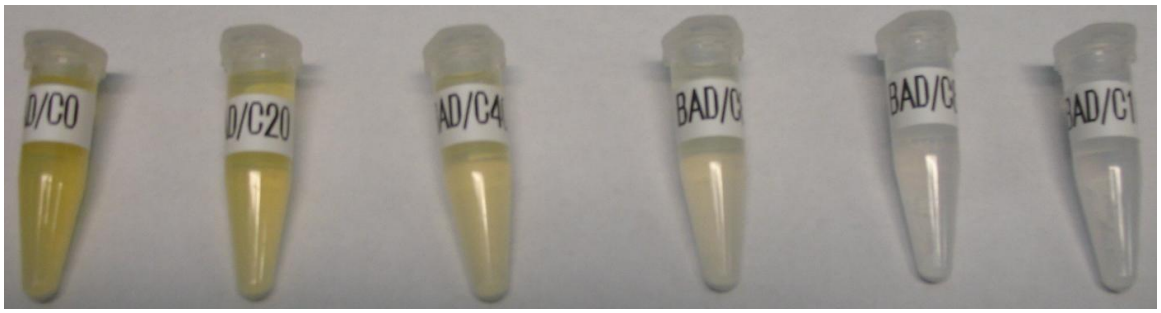

Figure 16: Sample B photocatalyst dye degradation.

UV-vis spectroscopy was used to measure methyl orange concentration as a function of time. Figure 17 below shows the UV-vis spectra using 5 ppm methyl orange/1000 ppm sample B solution. This trend is similar to what has been published elsewhere [51]. No shift in peak wavelength was observed in any spectra for all samples, and no new peaks formed.

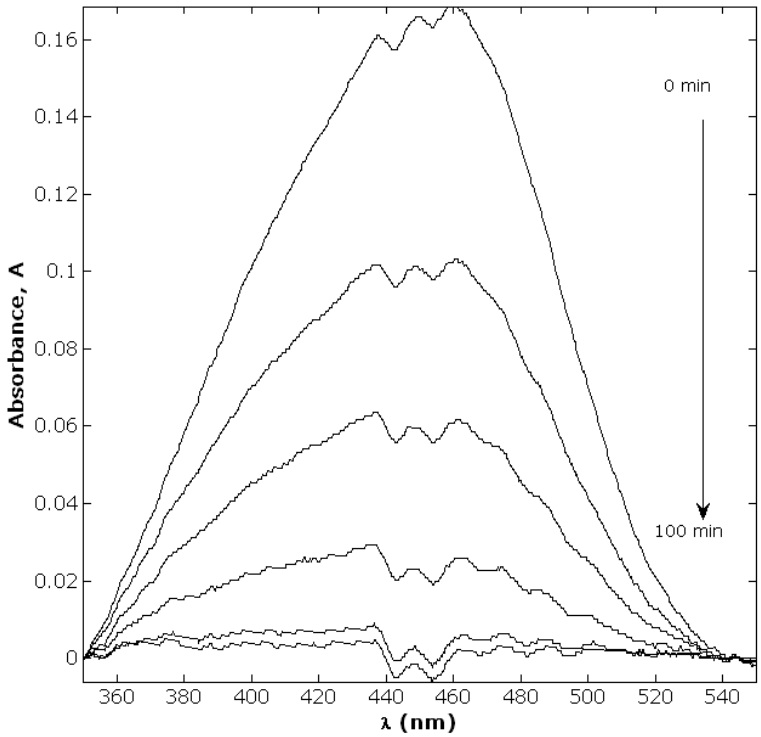

Figure 17: Time-progression of sample B absorption spectra.

The spectroscopy measurements were used to calculate relative absorbances (A/A0), which by Beer's law, are equivalent to relative concentrations (C/C_0). Figure 18 below shows A/A_0 vs. time for the 9 photocatalyst runs in table 9. The absorbance of the 450-nm peak was used, averaged over ± 15 nm. The error for each data point in figure 18 was approximated as the difference between the maximum and minimum absorbance in the 435-465 nm range, divided by two. Sample 5 degraded the fastest among the nine, reaching ≈85% decolorization in 100 minutes. There is an outlier present in the last measurement for sample 9, but the trend is clear regardless.

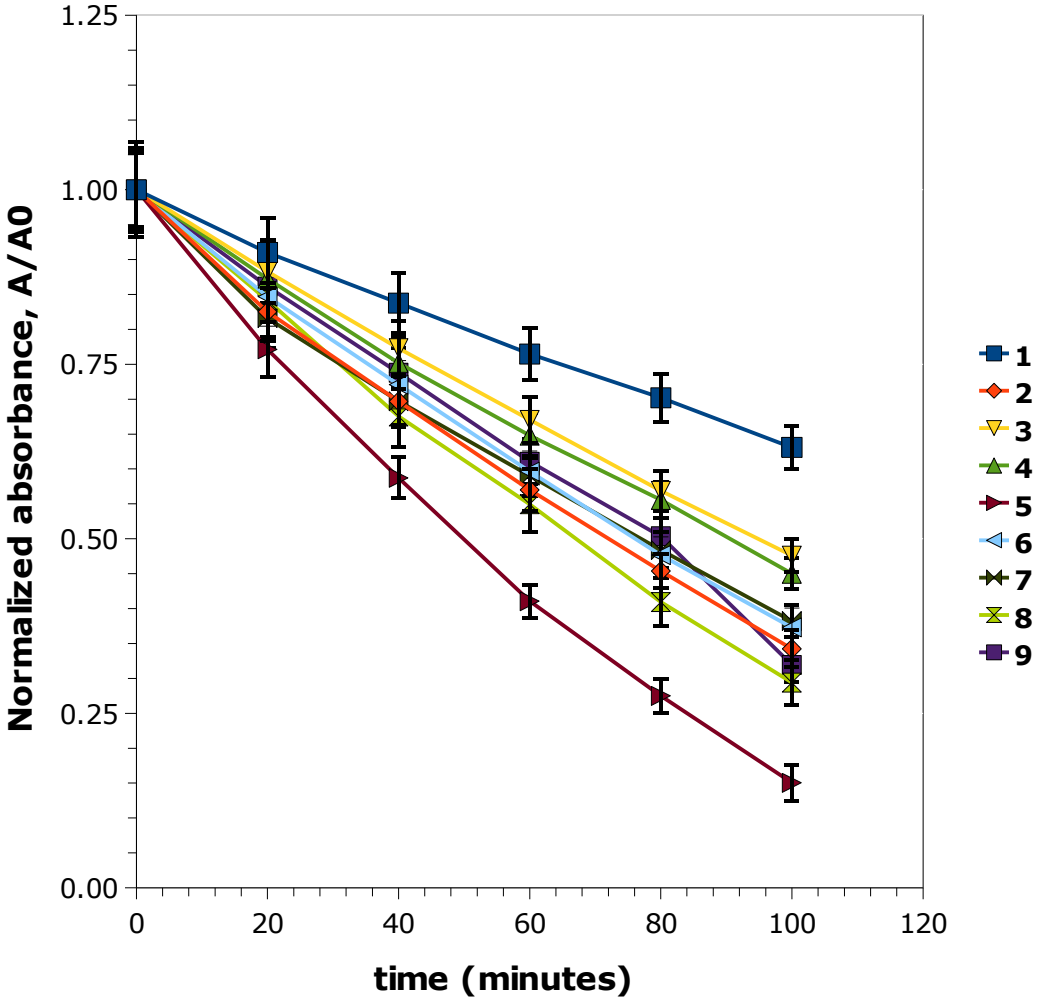

Figure 18: A/A_0 vs. time for the nine initial photocatalysts.

To calculate the reaction rate constants, the data were transformed to make a plot of ln(A/A0) vs. t for regression (figure 19 below). From this data, we conclude that the assumption of 1st-order kinetics was valid.

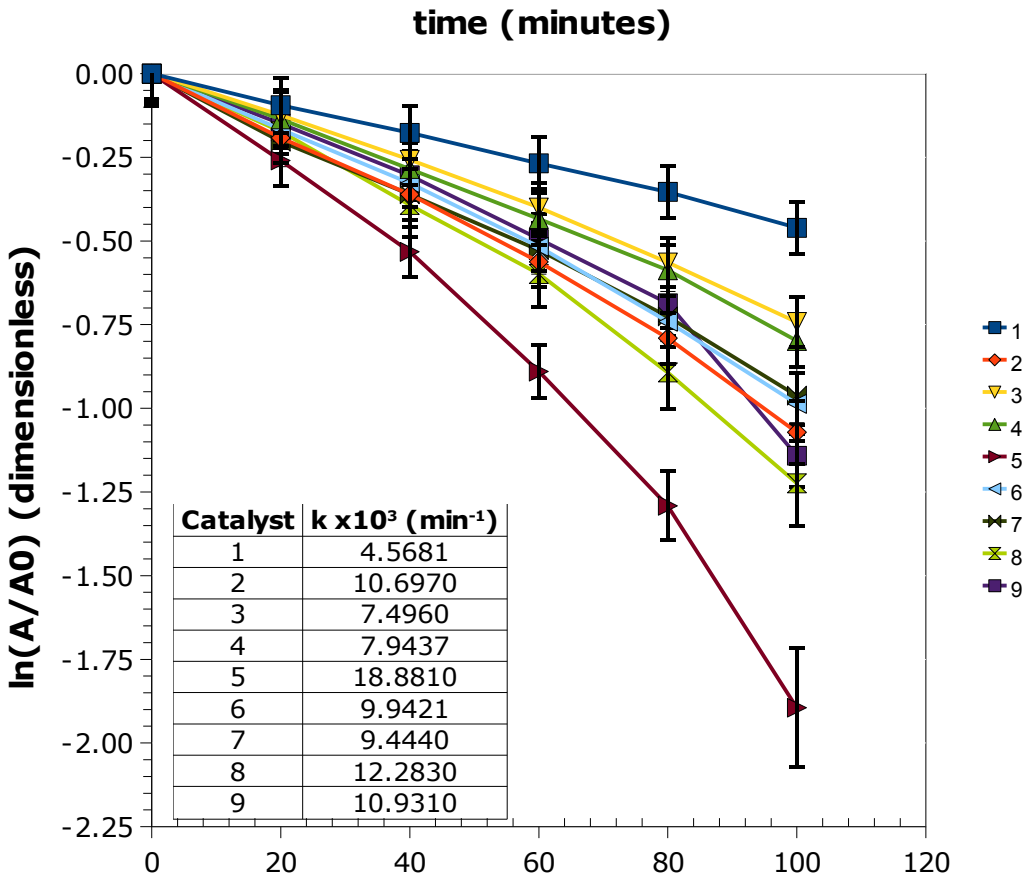

Figure 19: Natural logarithm of figure 18.

The regressed rate constants (inset of figure 19 above) were analyzed using the column-effects method (table 10 below):

Table 10: Column effects analysis of reaction rate constants.

		Levels			
		1	2	3	Max-min
Factors	w_{InVO4} (%)	7.5870	12.2556	10.8860	4.6686
	w_{Ni} (%)	7.3186	13.9537	9.4564	6.6351
	T_{calc} (°C)	8.9311	9.8572	11.9403	3.0093
	t_{mill} (hr)	11.4600	9.2409	10.0277	2.2191

The above results rank the order of importance as w_{Ni} > w_{In} > T_{calc} > t_{mill}. The data suggest that the fastest photocatalyst would have w_{InVO4} = 2%, w_{Ni} = 2%, T_{calc} = 800 °C, and t_{mill} = 4 hours. The worst possible catalyst preparation would have w_{InVO4} = 1%, w_{Ni} = 1%, T_{calc} = 600 °C, and t_{mill} = 12 hours. The ANOVA results in table 11 below suggests that w_{Ni} is the only significant variable (α = 10%). t_{mill} was used for estimating the error, since it was the weakest factor. The results parallel those of the column effects method, as expected.

Table 11: ANOVA of the regressed reaction rate constants.

Factor	Sum of Squares	df	Mean Squares	F	P(x>F)
w_{In} (%)	34.554	2	17.277	4.5496	0.1802
w_{Ni} (%)	68.820	2	34.410	9.0612	0.0994
T_{calc} (°C)	14.253	2	7.127	1.8766	0.3476
Error	7.595	2	3.7975		
Total	125.222	8			

The theoretical fastest and slowest catalyst preparations (samples A and B) were synthesized and tested. The results are shown in figure 20 below. The regressed rate constants were 30.8860 $x10^{-3}$ min^{-1} for A (r^2 = 0.95), and 57.1363 $x10^{-3}$ min^{-1} for B (r^2 = 0.84). Oddly, the slowest-predicted catalyst turned out to be the fastest, though both catalysts were substantially faster than the other nine.

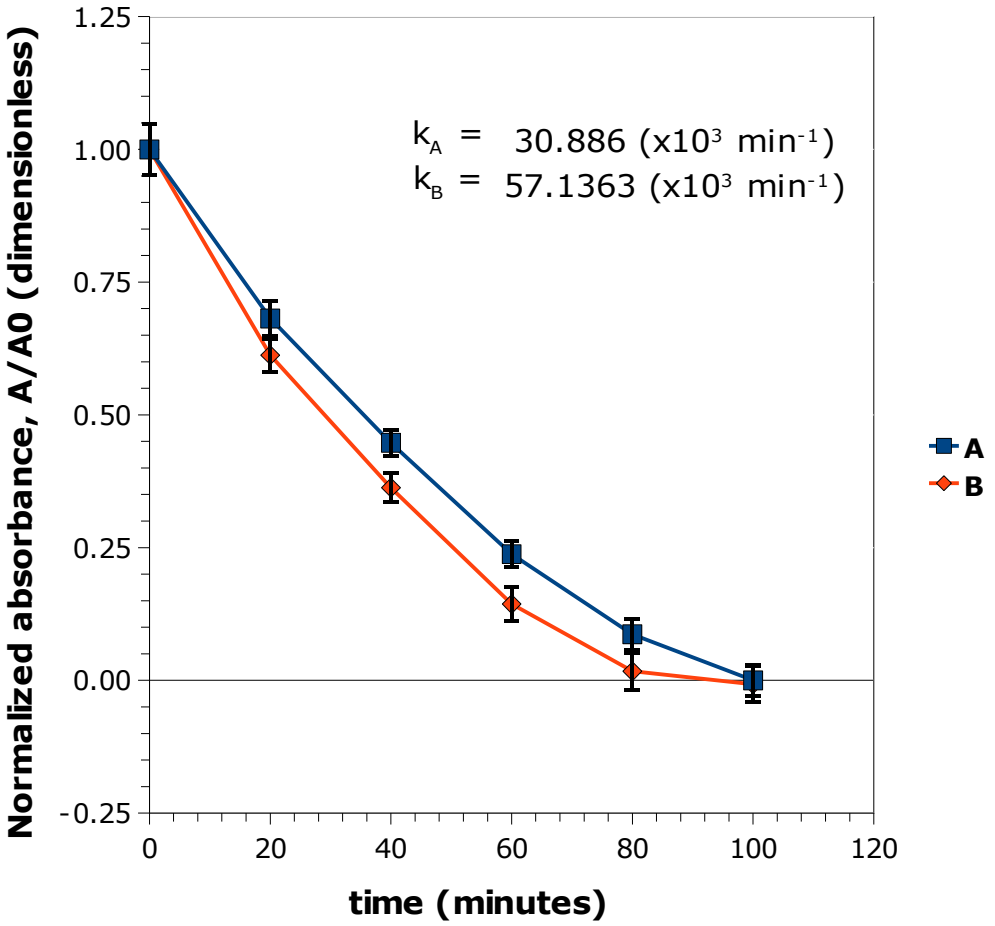

Figure 20: A/A_0 vs. time for samples A and B.

5.2 Catalyst Characterization Results

Catalyst run 1 (the slowest catalyst), and sample B (the fastest catalyst) were characterized in several ways. Since R1 and B had the greatest difference in reactivity, the physical differences responsible for this difference in reactivity should be easy to detect. For reference, the synthesis parameters for R1 and B are given in table 12 below:

Table 12: Synthesis parameters for catalysts R1 and B.

Parameter	*R1*	*B*
w_{Ni}	1%	1%
w_{InVO4}	1%	1%
T_{calc}	600	600
t_{mill}	4	12

Clearly, ball milling had a strong, positive effect on the reactivity of the photocatalyst. Figures 21 and 22 below shows SEM photographs of catalyst R1 and B, respectively, at progressively higher magnifications. There is a wide size distribution of roughly spherical particles, and the larger particles seem to be composed of fine particles that have agglomerated. There is little difference in size or shape between the two specimens, which suggests that the size of the particles reaches equilibrium within 4 hours of milling or less.

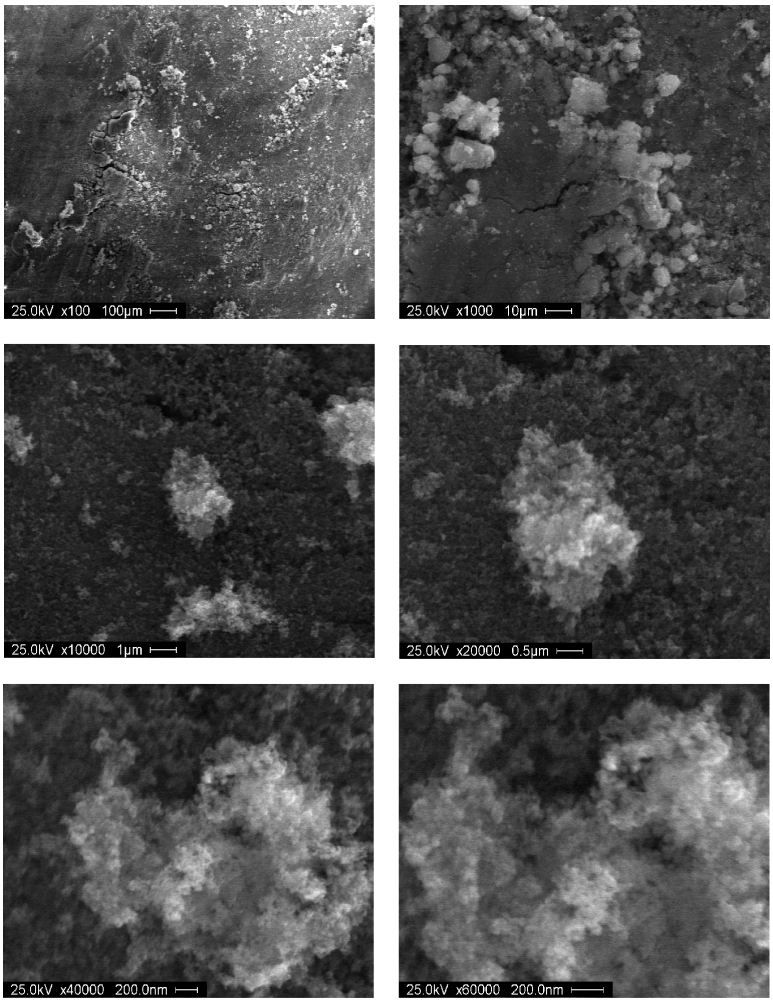

Figure 21: SEM photographs of catalyst R1.

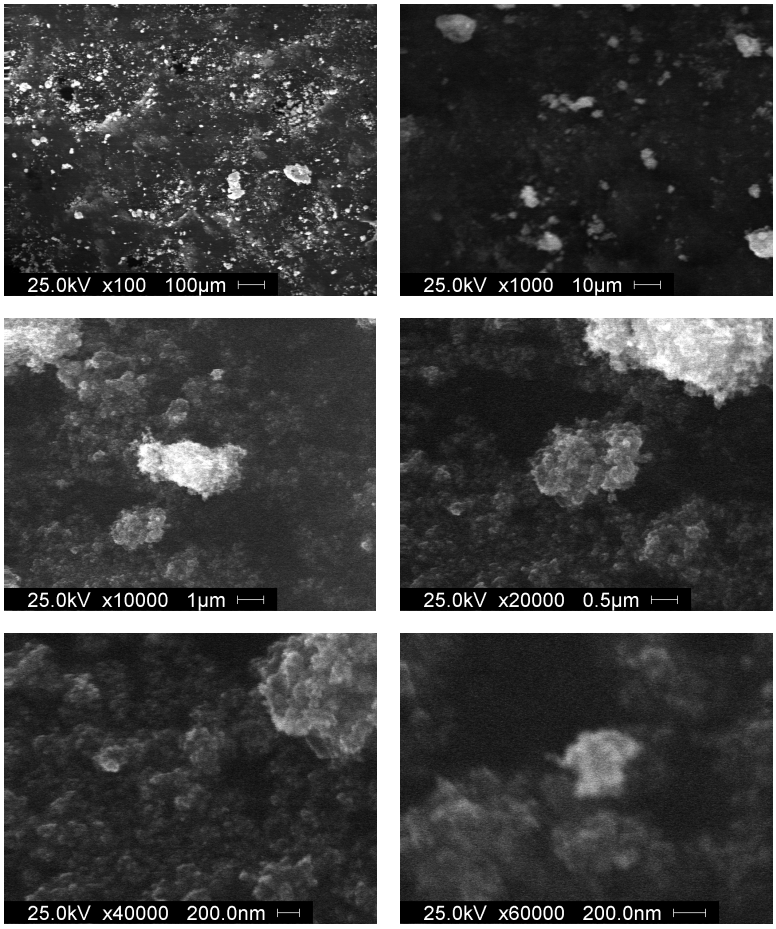

Figure 22: SEM photographs of catalyst B.

Both samples had a specific surface area of ~54 m^2/g. However, there is some difference between the pore size and pore volume data, shown in table 13 below:

Table 13: Surface area and pore size data for R1 and B.

	R1	B
Specific surface area (m^2/g)	53.6	54.8
Average pore diameter (nm)	14.9	17.6
Total pore volume (mL/g)	0.1992	0.2415

This data suggests that the greater pore size and pore volume could be a contributing factor to the greater reactivity of sample B, though the precise effect they would have on the reaction is hard to tell.

Figure 23 below shows x-ray powder diffractograms for run 1 and sample B, spaced at different heights for clarity. These peaks show representative peaks for TiO_2 (especially the large anatase peak at ~25 degrees). Nickel and $InVO_4$ however, are not readily visible, due to thin dispersion. The peaks were matched to the database stored in the PANalaytical X'Pert HighScore x-ray analysis software.

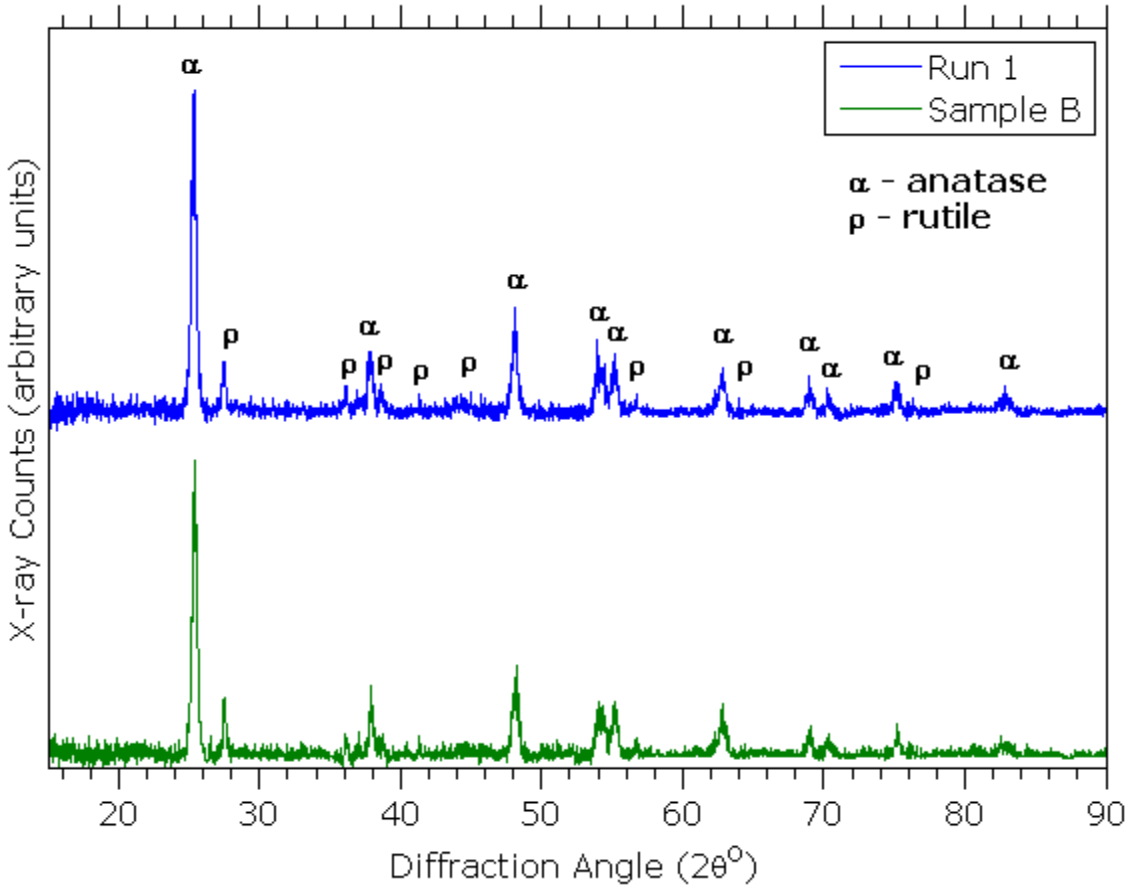

Figure 23: XRD patterns of catalysts R1 and B.

The Scherrer equation was used to find the average crystallite size, τ (Å):

$$\tau = \frac{K\lambda}{\beta \cos(\theta)} \tag{5}$$

Where K = 0.9 and λ is the wavelength of the x-ray source (1.54 Å). The other two arguments relate to a specific, chosen peak; in our case, we have chosen the intense anatase peak at 25.347° for crystallite size analysis. β is the full-width at half-maximum of the peak, and θ is the peak's position (divided by 2 to converted from 2θ to θ). Plugging in known values gave τ = 23 nm for both samples. High-magnification SEM photographs of the run 1 catalyst are shown in figure 24 below. The average size of these fine crystallites appears to be very close to the Scherrer prediction. These results are somewhat unexpected, since sample B was milled for 8 hours longer than run 1. We expected to see peak broadening, and prediction of a smaller crystallite size.

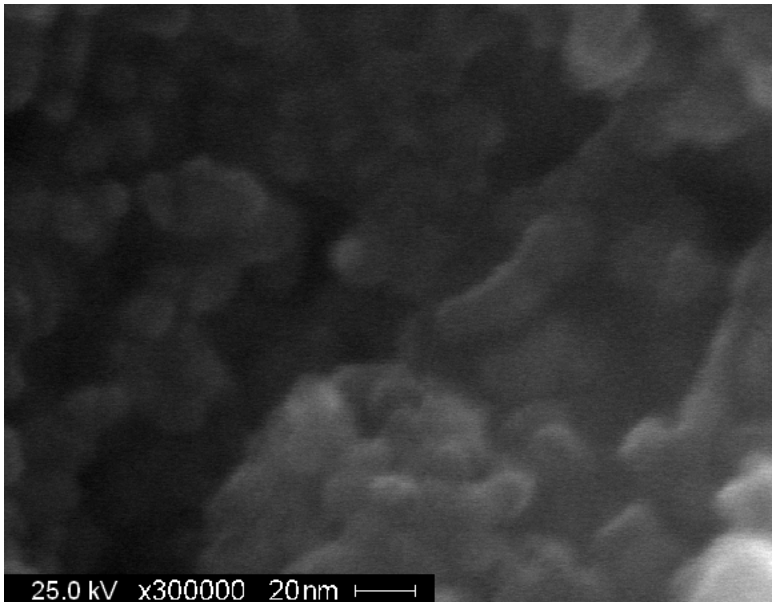

Figure 24: SEM image of R1 catalyst, 300,000x.

Figures 25 and 26 show EDS spectra for catalyst R1 and B, respectively. Due to the powder nature of the sample, the EDS results are only semi-quantitative. Elemental composition quantification results are given in tables 14 and 15. The quantification results do not appreciably detect vanadium, because Ti and V differ by only 1 atomic number. Indium however, was detected, despite some overlap with

the AgL peak. Carbon contamination appears slightly higher in sample R1.

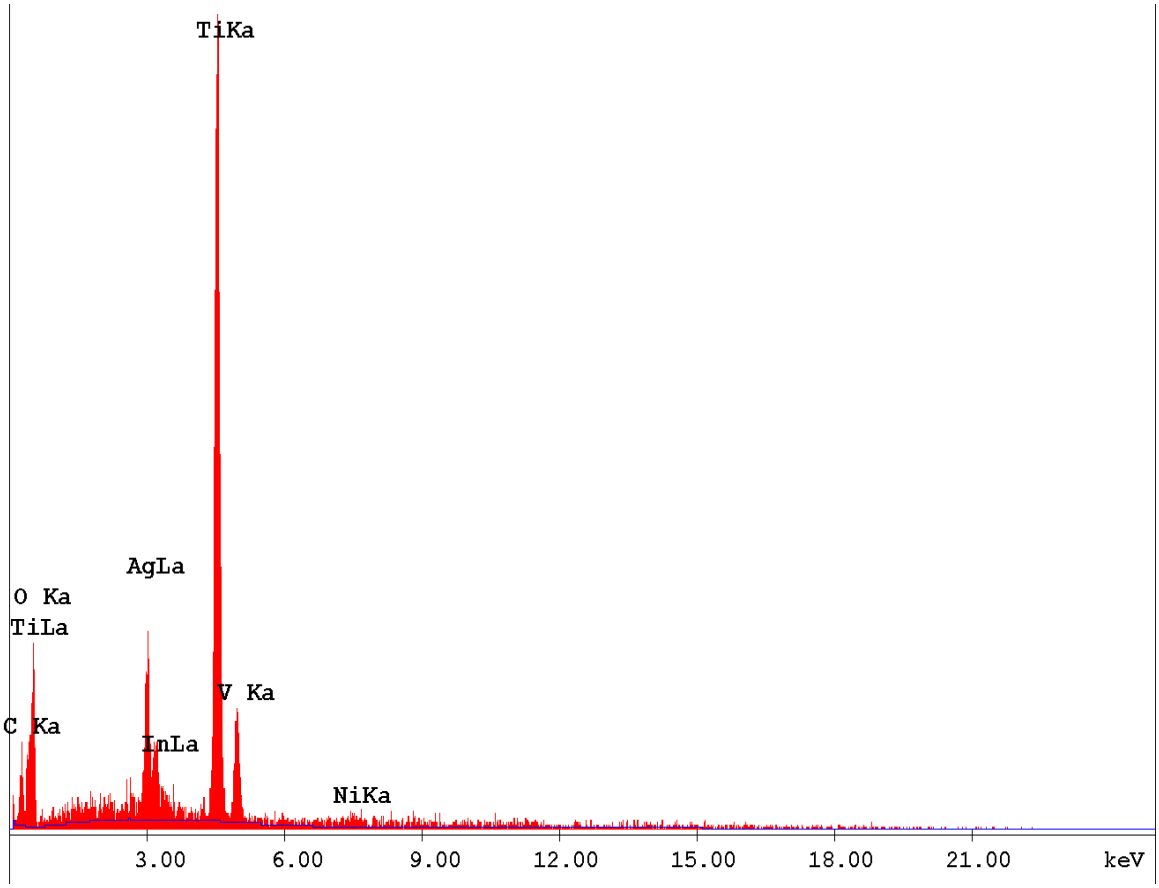

Figure 25: EDS spectrum for catalyst R1.

Table 14: EDS elemental quantification for catalyst R1.

EDAX ZAF Quantification (Standardless)
Element Normalized
SEC Table : Default

Element	Wt %	At %	K-Ratio	Z	A	F
C K	10.40	22.70	0.0401	1.1081	0.3480	1.0006
O K	30.14	49.41	0.0346	1.0911	0.1053	1.0001
AgL	13.30	3.23	0.1275	0.8415	1.1050	1.0313
InL	1.55	0.35	0.0151	0.8289	1.1239	1.0474
TiK	43.30	23.71	0.3805	0.9387	0.9354	1.0007
V K	0.00	0.00	0.0000	0.9202	0.9563	1.0011
NiK	1.31	0.59	0.0119	0.9572	0.9490	1.0000
Total	100.00	100.00				

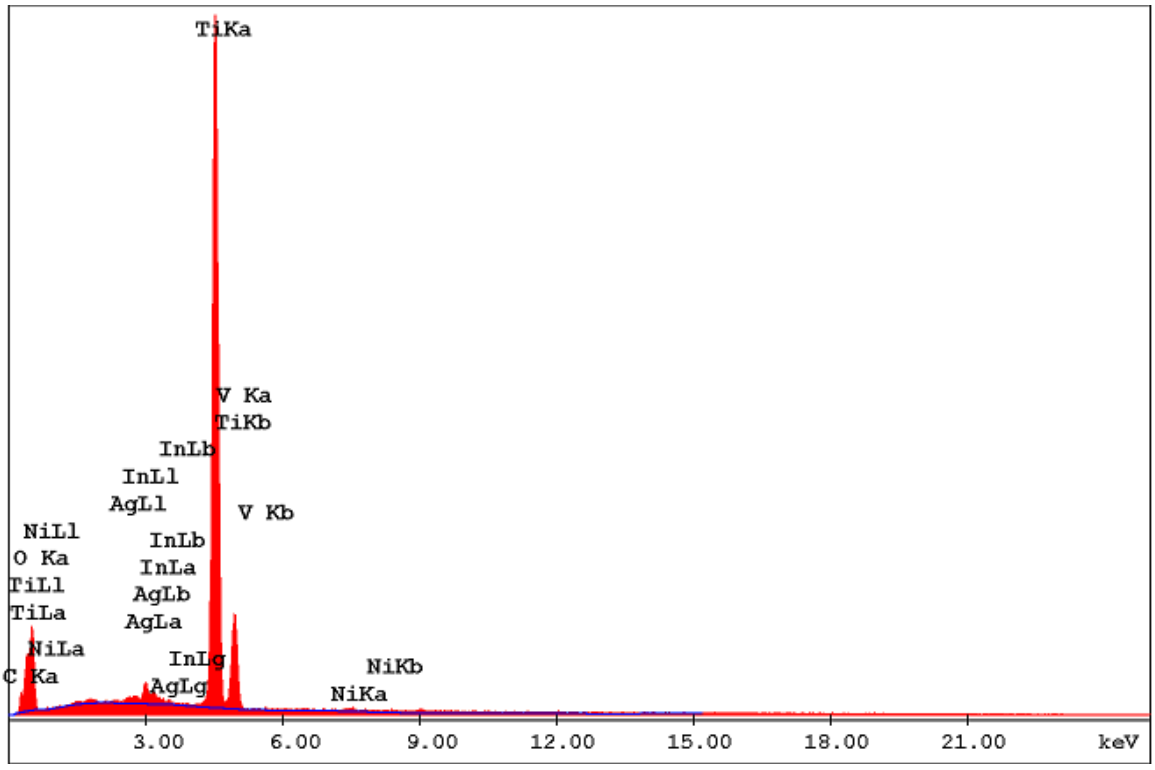

Figure 26: EDS spectrum for catalyst B.

Table 15: EDS elemental quantification for catalyst B.

EDAX ZAF Quantification (Standardless)
Element Normalized
SEC Table : Default

Element	Wt %	At %	K-Ratio	Z	A	F
C K	5.65	12.53	0.0199	1.1068	0.3186	1.0010
O K	32.50	54.10	0.0346	1.0897	0.0978	1.0001
AgL	2.55	0.63	0.0251	0.8385	1.1122	1.0580
InL	0.51	0.12	0.0052	0.8264	1.1302	1.0898
TiK	58.12	32.31	0.5419	0.9367	0.9950	1.0003
V K	0.12	0.06	0.0011	0.9183	1.0039	1.0005
NiK	0.55	0.25	0.0050	0.9541	0.9453	1.0000
Total	100.00	100.00				

Figures 27 (R1) and 28 (B) below show the EDS elemental maps used to view the spatial distribution of elements in the powders. The

secondary electron image in each figure is designated by "e^-." Both sets of maps show a homogeneous dispersion of all elements in the powder. However, since vanadium and titanium differ by only one electron, the vanadium elemental map is confounded with signals from the titanium atoms. This is not a great problem however. Since indium exists in the molecule $InVO_4$, there is one vanadium atom wherever there is one indium atom. Thus, the indium maps are a good indicator of indium and vanadium dispersion. The reader should not be distracted by the greater density of points on the sample B map, as there was some difficulty getting a similar amount of x-ray counts for the R1 catalyst maps. The important conclusion from the elemental maps is that the ball-milling has led to a uniform spatial dispersion of all elements in the sample.

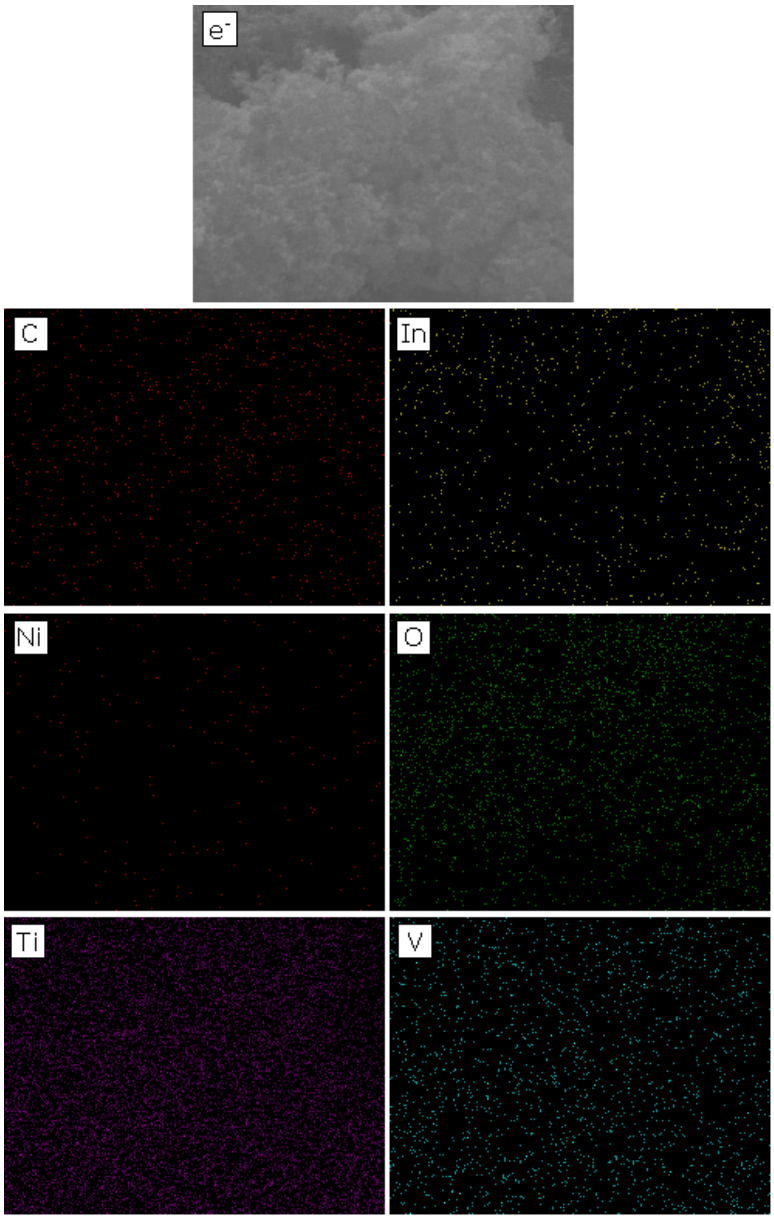

Figure 27: EDS elemental mapping for catalyst R1.

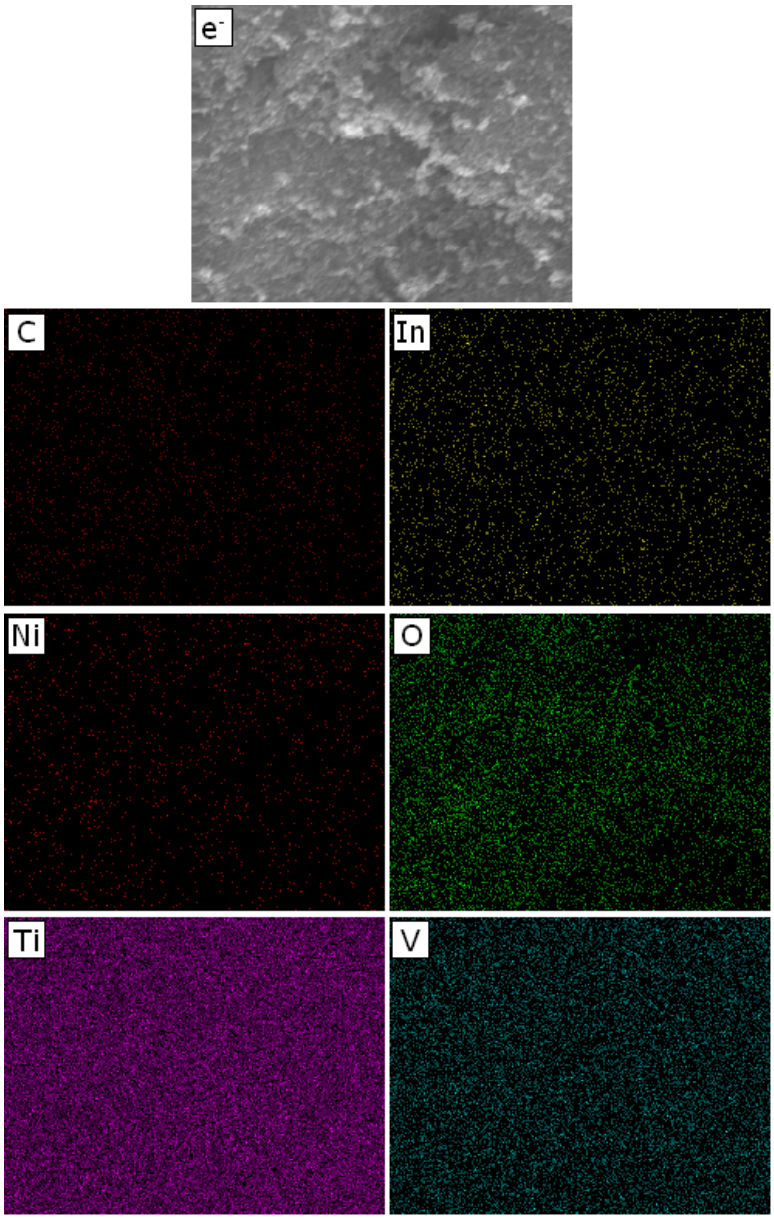

Figure 28: EDS elemental mapping for catalyst B.

Figure 29 below shows the diffuse reflectance spectroscopy (DRS) results for R1, B, and TiO_2. Greater absorbance in the visible is seen for catalysts R1 and B, due to the color centers introduced into the lattice from nickel doping. This is expected from the blue color change of the catalyst. Run 1's absorption edge has red-shifted from the pure TiO_2 by ~17 nm, while Sample B's has red-shifted ~27 nm.

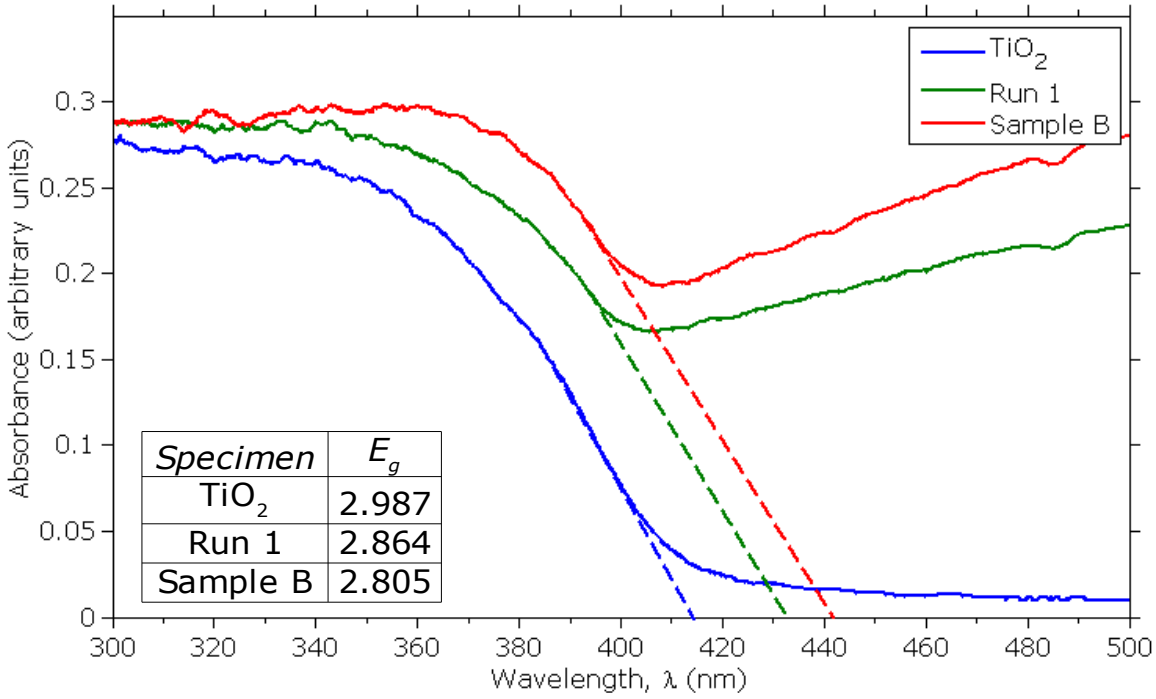

Figure 29: DRS spectra of TiO_2, R1, and B.

Red shifting of the band gap has been observed in the literature for samples of TiO_2 milled with metals and nitrogen [52-54]. The likely explanation for the red shift is that the nickel dopant has inserted extra energy levels into the band gap close to the valence band, which has decreased the amount of energy required for the jump to the conduction band.

5.3 Discussion

The effect of $InVO_4$ at the tested concentrations and calcination temperatures appears to be very weak. The optimum synthesis parameters for the photocatalyst can be summarized simply as "low amounts of nickel and long milling time." However, there is disagreement between our statistical analysis and the final results. Tables 10 and 11 suggested that milling time was the least-important (and statistically insignificant) parameter. However, the only difference in synthesis treatment between samples R1 and B was greater milling time. Clearly, milling time is not insignificant when nickel concentration is low.

The most likely reason is that there is a strong interaction effect between nickel concentration and milling time, which our OA design did not consider. One hypothesis is that the greater milling time has increased the conversion of Ni-doped TiO_2. Greater milling time would logically increase this yield, since this would increase the probability that a ball in the mill would collide with a particle of TiO_2 and Ni to cause the doping. It is difficult to see if this is the case with our catalyst, since the powder form of the catalyst has dulled the precision of the EDS quantification results. More precise methods, such as XPS or SIMS, could detect these differences.

The large size of the catalyst particles is the likely reason that low nickel concentration is favored. Studies by Zhang et al [55] showed that as particle size increases, the concentration of Fe^{3+} required for optimum photocatalytic reactivity decreases dramatically. Surface h_{vb}^{+}-trapping states are the active sites for this type of reaction. It is desirable to keep h_{vb}^{+} trapped in these states for as long as possible, since this increases the chance that photoreaction will occur. The addition of dopants creates trapping centers in the bulk of the material, which slow the migration of e_{cb}^{-} to the surface. Ideally, opposing charge carriers would be separated for the exact amount of time required for a reaction, thus ensuring no recombination occurs. In the larger particle, the charge carriers generated in the bulk have a longer path to travel to reach the surface, and thus do not need to be slowed as greatly. For this reason, lower amounts of doping are favored.

In the smaller catalyst particle however, the path length to the surface is much smaller. Because of this, a greater dopant concentration is required to separate the charge carriers. Zhang's study showed that TiO_2 particles between 10 and 20 nm favored low (~0.1 atomic %) amounts of Fe^{3+} dopant, while particles < 10 nm in size favored greater concentrations. From our SEM images, our particles are generally larger than 20 nm, thus it makes sense that reactivity should increase with decreasing nickel concentration.

Chapter 6: Conclusions and Future Work

6.1 Conclusions

i. The InVO4 concentrations and calcination temperatures tested had no discernible effect on the reactivity of the photocatalyst.
ii. Nickel concentration was a significant (90% confidence) variable, and it seems to have a strong, positive interaction effect with the milling time.
iii. The settings of the fastest photocatalyst were w_{Ni} = 1%, w_{InVO4} = 1%, T_{calc} = 600 °C, and t_{mill} = 12 hours. High reactivity favored low amounts of nickel and long milling time. Lower nickel concentration is likely optimal due to the larger size of our TiO_2 particles.
iv. The physical properties of the catalyst that are likely responsible for the faster reactivity of the optimum photocatalyst are its narrower band gap (~442 nm), as well as its slightly larger average pore diameter and total pore volume.

6.2 Future Work

TiO_2 has been studied since the 1970's for use as a photocatalyst, but overall, the results of the research effort is mixed. Despite many successful attempts to reduce the band gap, the catalyst only possesses a certain amount of quantum efficiency, which for pure TiO_2 is capped at ~10% [23]. Considering that the economic feasibility of any photocatalytic treatment process is directly dependent on the quantum efficiency, it is probably best to investigate other photocatalysts that have greater quantum efficiency than TiO_2, even if they are more expensive.

It could also be worthwhile to rethink the reactions being investigated. Wastewater remediation is a noble goal, but the present energy crisis has driven the need for a cheap, renewable replacement for gasoline as an automotive fuel. Especially attractive is the possibility of using natural sunlight to activate a photocatalyst for the reduction of CO_2 to methanol. $InVO_4$ has been demonstrated to split water into $H_2 + O_2$, and reduce CO_2 to CH_3OH. These considerations merit further exploration of the $InVO_4$ system.

There are also many possible factors related to the type of reactor and the reaction conditions, which we did not investigate in this work. Though in this study a slurry reactor was used, fixed-bed setups have many advantages, the most important one being that the need for solid-liquid separation is avoided. Such a system would be ideal for exploring methanol conversion, since the reaction products could be fed directly into a gas chromatograph/mass spectrometer without needing to filter out the solids.

References

[1] D. Finney, *An introduction to the theory of experimental design*, Chicago: University of Chicago, 1960.

[2] J.F. Louvar, "Simplify Experimental Design," *Chemical Engineering Progress*, vol. 106, 2010, pp. 35-40.

[3] P.J. Ross, *Taguchi Techniques for Quality Engineering*, New York: McGraw-Hill, 1996.

[4] A. Hedayat, N. Sloane, and J. Stufken, *Orthogonal Arrays: Theory and Applications*, New York: Springer, 1999.

[5] N. Sloane, "A Library of Orthogonal Arrays," http://www2.research.att.com/~njas/oadir/. 2009.

[6] L. Ge, M. Xu, and H. Fang, "Photo-catalytic degradation of methyl orange and formaldehyde by Ag/InVO4-TiO2 thin films under visible-light irradiation," *Journal of Molecular Catalysis A: Chemical*, vol. 258, Oct. 2006, pp. 68-76.

[7] L. Ge, M. Xu, and H. Fang, "Synthesis and characterization of the Pd/InVO4-TiO2 co-doped thin films with visible light photocatalytic activities," *Applied Surface Science*, vol. 253, Dec. 2006, pp. 2257-2263.

[8] L. Ge, M. Xu, and H. Fang, "Synthesis of novel photocatalytic InVO4-TiO2 thin films with visible light photoactivity," *Materials Letters*, vol. 61, Jan. 2007, pp. 63-66.

[9] Z. Zhao, J. Fan, S. Liu, and Z. Wang, "Optimal design and preparation of titania-supported CoPc using sol-gel for the photo-reduction of CO2," *Chemical Engineering Journal*, vol. 151, Aug. 2009, pp. 134-140.

[10] C. MARCILLY, P. COURTY, and B. DELMON, "Preparation of Highly Dispersed Mixed Oxides and Oxide Solid Solutions by Pyrolysis of Amorphous Organic Precursors," *Journal of the American Ceramic Society*, vol. 53, 1970, pp. 56-57.

[11] L. Zhang, H. Fu, C. Zhang, and Y. Zhu, "Synthesis, characterization, and photocatalytic properties of InVO4 nanoparticles," *Journal of Solid State Chemistry*, vol. 179, Mar. 2006, pp. 804-811.

[12] A.J. van Dillen, R.J.A.M. Terorde, D.J. Lensveld, J.W. Geus, and K.P. de Jong, "Synthesis of supported catalysts by impregnation and drying using aqueous chelated metal complexes," *Journal of Catalysis*, vol. 216, May, pp. 257-264.

[13] N. Sloane, "L9 Orthogonal Array," Jan. 2010. http://www2.research.att.com/~njas/oadir/

[14] C. Kittel, *Introduction to Solid State Physics*, New York: Wiley, 1996.

[15] W. Beam, *Electronics of Solids*, New York: McGraw-Hill, 1965.

[16] M. Yoder, "Wide bandgap semiconductor materials and devices," *Electron Devices, IEEE Transactions on*, vol. 43, 1996, pp. 1633-1636.

[17] C.R. Nave, "Band Theory of Solids ," *Georgia State University HyperPhysics*, 2005.

[18] M. Gratzel, *Heterogeneous Photochemical Electron Transfer*, Boca Raton: CRC Press, 1989.

[19] B. Van Zeghbroeck, "Carrier generation and recombination," *Principles of Semiconductor Devices*, 2007.

[20] T. Nguyen and A.R. Hind, "The measurement of absorption edge and band gap properties of novel nanocomposite materials," *Varian Australia*, vol. 81, pp. 1-5.

[21] H. Lachheb, E. Puzenat, A. Houas, M. Ksibi, E. Elaloui, C. Guillard, and J. Herrmann, "Photocatalytic degradation of various types of dyes (Alizarin S, Crocein Orange G, Methyl Red, Congo Red, Methylene Blue) in water by UV-irradiated titania," *Applied Catalysis B: Environmental*, vol. 39, Nov. 2002, pp. 75-90.

[22] I.K. Konstantinou and T.A. Albanis, "TiO2-assisted photocatalytic degradation of azo dyes in aqueous solution: kinetic and mechanistic investigations: A review," *Applied Catalysis B: Environmental*, vol. 49, Apr. 2004, pp. 1-14.

[23] D. Beydoun, R. Amal, G. Low, and S. McEvoy, "Role of Nanoparticles in Photocatalysis," *Journal of Nanoparticle Research*, vol. 1, Dec. 1999, pp. 439-458.

[24] D.S. Bhatkhande, V.G. Pangarkar, and A.A. Beenackers, "Photocatalytic degradation for environmental applications - a review," *Journal of Chemical Technology & Biotechnology*, vol. 77, 2002, pp. 102-116.

[25] J. Herrmann, "Heterogeneous photocatalysis: fundamentals and applications to the removal of various types of aqueous pollutants," *Catalysis Today*, vol. 53, Oct. 1999, pp. 115-129.

[26] M.R. Hoffmann, S.T. Martin, W. Choi, and D.W. Bahnemann, "Environmental Applications of Semiconductor Photocatalysis," *Chemical Reviews*, vol. 95, Jan. 1995, pp. 69-96.

[27] A.L. Linsebigler, G. Lu, and J.T. Yates, "Photocatalysis on TiO2 Surfaces: Principles, Mechanisms, and Selected Results," *Chemical Reviews*, vol. 95, May. 1995, pp. 735-758.

[28] M.A. Fox and M.T. Dulay, "Heterogeneous photocatalysis," *Chemical Reviews*, vol. 93, Jan. 1993, pp. 341-357.

[29] A. Mills and S. Le Hunte, "An overview of semiconductor photocatalysis," *Journal of Photochemistry and Photobiology A: Chemistry*, vol. 108, Jul. 1997, pp. 1-35.

[30] U.N. Center for Computational Materials Science, "The Anatase (C5) Structure." http://cst-www.nrl.navy.mil/lattice/struk/c5.html

[31] U.N. Center for Computational Materials Science, "The Rutile (C4) Structure," *Naval Research Laboratory*. http://cst-www.nrl.navy.mil/lattice/struk/c4.html.

[32] U.N. Center for Computational Materials Science, "The Brookite (C21) Structure," *Naval Research Laboratory*. http://cst-www.nrl.navy.mil/lattice/struk/c21.html

[33] F. Dachille, P. Simons, and R. Rustum, "PRESSURE-TEMPERATURE STUDIES OF ANATASE, BROOKITE, RUTILE AND TiO,-II," *The American Mineralogist*, vol. 53, 1968, pp. 1929-1939.

[34] Z. Zou and H. Arakawa, "Direct water splitting into H2 and O2 under visible light irradiation with a new series of mixed oxide semiconductor photocatalysts," *Journal of Photochemistry and Photobiology A: Chemistry*, vol. 158, Jun. 2003, pp. 145-162.

[35] J. Ye, Z. Zou, M. Oshikiri, A. Matsushita, M. Shimoda, M. Imai, and T. Shishido, "A novel hydrogen-evolving photocatalyst InVO4 active under visible light irradiation," *Chemical Physics Letters*, vol. 356, Apr. 2002, pp. 221-226.

[36] H. Lin, Y. Chen, and Y. Chen, "Water splitting reaction on NiO/InVO4 under visible light irradiation," *International Journal of Hydrogen Energy*, vol. 32, Jan. 2007, pp. 86-92.

[37] J. Ye, Z. Zou, H. Arakawa, M. Oshikiri, M. Shimoda, A. Matsushita, and T. Shishido, "Correlation of crystal and electronic structures with photophysical properties of water splitting photocatalysts InMO4 (M=V5+,Nb5+,Ta5+)," *Journal of Photochemistry and Photobiology A: Chemistry*, vol. 148, May. 2002, pp. 79-83.

[38] I.B. Afanas'ev, *Superoxide Ion: Chemistry and Biological Implications*, Boca Raton: CRC Press, 1991.

[39] C. Suryanarayana, E. Ivanov, and V.V. Boldyrev, "The science and technology of mechanical alloying," *Materials Science and Engineering A*, vol. 304-306, May. 2001, pp. 151-158.

[40] P.G. McCormick, T. Tsuzuki, J.S. Robinson, and J. Ding, "Nanopowders Synthesized by Mechanochemical Processing," *Advanced Materials*, vol. 13, 2001, pp. 1008-1010.

[41] C. Suryanarayana, "Mechanical alloying and milling," *Progress in Materials Science*, vol. 46, Jan. 2001, pp. 1-184.

[42] G. Le Caër, P. Delcroix, S. Bégin-Colin, and T. Ziller, "High-Energy Ball-Milling of Alloys and Compounds," *Hyperfine Interactions*, vol. 141-142, Jun. 2002, pp. 63-72.

[43] H. Mio, J. Kano, F. Saito, and K. Kaneko, "Effects of rotational direction and rotation-to-revolution speed ratio in planetary ball milling," *Materials Science and Engineering A*, vol. 332, Jul. 2002, pp. 75-80.

[44] S. Indris, D. Bork, and P. Heitjans, "Nanocrystalline Oxide Ceramics Prepared by High-Energy Ball Milling," *Journal of Materials Synthesis and Processing*, vol. 8, Jul. 2000, pp. 245-250.

[45] C. Shifu, C. Lei, G. Shen, and C. Gengyu, "The preparation of coupled SnO2/TiO2 photocatalyst by ball milling," *Materials Chemistry and Physics*, vol. 98, Jul. 2006, pp. 116-120.

[46] D.H. Kim, K.S. Lee, Y. Kim, Y. Chung, and S. Kim, "Photocatalytic Activity of Ni 8 wt%-Doped TiO₂ Photocatalyst Synthesized by Mechanical Alloying Under Visible Light," *Journal of the American Ceramic Society*, vol. 89, 2006, pp. 515-518.

[47] Z. Zhang, C. Wang, R. Zakaria, and J.Y. Ying, "Role of Particle Size in Nanocrystalline TiO2-Based Photocatalysts," *The Journal of Physical Chemistry B*, vol. 102, Dec. 1998, pp. 10871-10878.

[48] J. Szanics and M. Kakihana, "A Novel Tantalic Acid-Based Polymerizable Complex Route to LiTaO3 Using Neither Alkoxides nor Chlorides of Tantalum," *Chemistry of Materials*, vol. 11, Oct. 1999, pp. 2760-2763.

[49] S. Zhang, C. Zhang, H. Yang, and Y. Zhu, "Formation and performances of porous InVO4 films," *Journal of Solid State Chemistry*, vol. 179, Mar. 2006, pp. 873-882.

[50] C.A. Coutinho and V.K. Gupta, "Photocatalytic degradation of methyl orange using polymer-titania microcomposites," *Journal of Colloid and Interface Science*, vol. 333, May. 2009, pp. 457-464.

[51] S. Al-Qaradawi and S.R. Salman, "Photocatalytic degradation of methyl orange as a model compound," *Journal of Photochemistry and Photobiology A: Chemistry*, vol. 148, May. 2002, pp. 161-168.

[52] D.H. Kim, H.S. Hong, S.J. Kim, J.S. Song, and K.S. Lee, "Photocatalytic behaviors and structural characterization of nanocrystalline Fe-doped TiO2 synthesized by mechanical alloying," *Journal of Alloys and Compounds*, vol. 375, Jul. 2004, pp. 259-264.

[53] Y.R. Uhm, S.H. Woo, W.W. Kim, S.J. Kim, and C.K. Rhee, "The characterization of magnetic and photo-catalytic properties of nanocrystalline Ni-doped TiO2 powder synthesized by mechanical alloying," *Journal of Magnetism and Magnetic Materials*, vol. 304, Sep. 2006, pp. e781-e783.

[54] S. Yin, H. Yamaki, M. Komatsu, Q. Zhang, J. Wang, Q. Tang, F. Saito, and T. Sato, "Synthesis of visible-light reactive TiO2-xNy photocatalyst by mechanochemical doping," *Solid State Sciences*, vol. 7, Dec. 2005, pp. 1479-1485.

[55] Z. Zhang, C. Wang, R. Zakaria, and J.Y. Ying, "Role of Particle Size in Nanocrystalline TiO2-Based Photocatalysts," *The Journal of Physical Chemistry B*, vol. 102, Dec. 1998, pp. 10871-10878.

[56] StatSoft, Inc. Electronic Statistics Textbook, "ANOVA/MANOVA." http://www.statsoft.com/textbook/anova-manova/.

[57] H.M. Wadsworth, *Handbook of statistical methods for engineers and scientists: Probability Distributions and Statistical Inference*, New York: McGraw-Hill.

[58] H.M. Wadsworth, *Handbook of statistical methods for engineers and scientists: Appendix*, New York: McGraw-Hill.

Appendices

Appendix A: The F-Test and Two-Way ANOVA

Significance tests, such as the two-sample t-test, are standard statistical inference tools. Such tests however, are inefficient for testing multiple variables simultaneously. A better method, analysis of variance (ANOVA), tests whether the variation in the data contributed by a factor is statistically greater than that contributed by the random (unexplainable) error. Despite using the variance between samples, the ANOVA is actually a test of significance for means [56].

Before the ANOVA procedure is discussed, it is helpful to have some background on the F-test. The *F*-test tells whether the variances of two normally-distributed populations are statistically equal [57]. Assuming equal variances, the *F*-statistic is:

$$F = \frac{s_1^2}{s_2^2} \tag{6}$$

If samples 1 and 2 are normally distributed, then the test statistic, *F*, is drawn from an *F* distribution, with degrees of freedom df_1 and df_2, respectively. The critical *F*-value (F*) is a function of df_1, df_2, and the significance level, α. Consider the data below:

Table 16: Example data set for F-test.

$\mathbf{x_1}$	7	14	-7	9	6	-2	2	6	22	18
$\mathbf{x_2}$	-6	29	10	4	10	3	4	16	16	16

Samples x_1 and x_2 have $s_1^2 = 77.8333$ and $s_2^2 = 93.9556$, respectively. Both samples have n = 10, and thus $df_1 = df_2 = (10 - 1) = 9$. From this data, $F = 77.8333/93.9556 = 0.8284$. The critical F-value tables in Wadsworth [58] give $F^*_{0.05,9,9} = 3.18$. Since $F < F^*$, we conclude that the variances between the two samples are statistically indistinguishable at the 5% significance level.

The example below will give the reader an idea of how a two-factor ("two-way") ANOVA is performed. Suppose we have a reaction whose product yield (in mmol), is dependent on temperature and pH. Three levels for the two factors were chosen, and four trials performed for each treatment. Table 17 below gives the results.

Table 17: Two-way ANOVA table example data.

		T (°C)					
		25		50		75	
pH	2	5.512	6.320	6.946	5.629	5.755	6.281
		6.717	6.190	5.957	5.507	5.080	6.370
	7	5.422	5.645	5.404	6.139	5.025	6.721
		6.690	6.264	6.143	6.564	6.535	5.682
	12	5.779	5.719	5.668	6.138	5.911	5.626
		6.636	6.378	6.148	6.914	6.190	5.229

We denote the elements in the table by X_{ijk}, where i is the row index, j is the column index, and k is the index of the elements in the cell-ij. We use a summation convention, denoted by $X_{ij\bullet}$, where • means "averaged over this index." For example, $X_{ij\bullet}$ is the average value of cell-ij. The "grand mean" of all elements is $X_{\bullet\bullet\bullet}$. To do the ANOVA, we assume each X_{ijk} is drawn from an $N(\mu_{ij}, \sigma)$ distribution; that is, the cell means may be different, but the cell variances are equal. This assumption can be tested with an F-test on the two cells with the greatest difference in variance. Table 18 below shows the nine $X_{ij\bullet}$, three $X_{i\bullet\bullet}$, and three $X_{\bullet j\bullet}$.

Table 18: Table of cell, row, and column averages of table 17.

		T (°C)			
		25	50	75	
pH	2	6.185	6.010	5.871	6.022
	7	6.005	6.063	5.991	6.019
	12	6.128	6.217	5.739	6.028
		6.106	6.096	5.867	**6.023**

$X_{i\bullet\bullet}$

$X_{\bullet j\bullet}$

Grand mean, $X_{\bullet\bullet\bullet}$

Appendix A (Continued)

Unlike the previous example with samples x_1 and x_2, we do not use "actual" variances in the ANOVA test. Instead, we use an indirect measure of variance, called sum-of-square (SS). To do the ANOVA, we calculate several SS values, and each one represents a portion of the total variation. There is one SS value for each factor (in this case, SS_T and SS_{pH}) , each interaction ($SS_{pH,T}$) , and one for the cell error (SS_e). Adding these components gives the total variation, defined by:

$$SS_{total} = SS_A + SS_B + SS_{AB} + SS_e$$

The different SS values are given by the equations below [57]:

$$SS_A = Jn\sum_{i=1}^{I}(X_{i\bullet\bullet} - X_{\bullet\bullet\bullet})^2 \tag{7}$$

$$SS_B = In\sum_{j=1}^{J}\left(X_{\bullet j\bullet} - X_{\bullet\bullet\bullet}\right)^2 \tag{8}$$

$$SS_{AB} = n\sum_{i=1}^{I}\sum_{j=1}^{J}\left(X_{ij\bullet} - X_{i\bullet\bullet} - X_{\bullet j\bullet} + X_{\bullet\bullet\bullet}\right)^2 \tag{9}$$

$$SS_e = \sum_{i=1}^{I}\sum_{j=1}^{J}\sum_{k=1}^{n}\left(X_{ijk} - X_{ij\bullet}\right)^2 \tag{10}$$

Appendix A (Continued)

$$SS_{tot} = \sum_{i=1}^{I} \sum_{j=1}^{J} \sum_{k=1}^{n} \left(X_{ijk} - X_{\bullet\bullet\bullet}\right)^2 \qquad (11)$$

The calculated SS values are:

SS_{pH} = 0.000449
SS_T = 0.43913
$SS_{pH,T}$ = 0.2869
SS_e = 8.561
SS_{tot} = 9.2868

We now calculate the mean squares (MS), which are the sum-of-squares terms divided by their corresponding degrees-of-freedom:

df_{pH} = (I – 1) = 2, $MS_{pH} = SS_{pH}/df_{pH}$ = 0.000449/2 = 0.0002245
df_T = (J – 1) = 2, $MS_T = SS_T/df_T$ = 0.43913/2 = 0.21957
$df_{pH,T}$ = (I – 1)(J – 1) = 4, $MS_{pH,T} = SS_{pH,T}/df_{pH,T}$ = 0.2869/4 = 0.071725
df_e = IJ(n – 1) = 27, $MS_e = SS_e/df_e$ = 8.561/27 = 0.31707
df_{tot} = IJn - 1 = 35

Note that df_{tot} is the sum of all the other df's. We then divide all other MS-values by the mean-square-error, MS_e. The F-statistics for the pH, temperature, and interaction are:
F_{pH} = 0.0002245/0.31707 = 0.00070805
F_T = 0.21957/0.31707 = 0.6925
$F_{pH,T}$ = 0.071725/0.31707 = 0.22621

The 5% critical F values are:

$F^*_{pH} = F_{0.05,2,27}$ = 3.35
$F^*_T = F_{0.05,2,27}$ = 3.35
$F^*_{pH,T} = F_{0.05,4,27}$ = 2.73

Since F < F* for each comparison, we conclude, with 95% confidence, that the effect of pH and temperature on the reaction is insignificant,

and that there is no significant interaction effect between pH and temperature.